

©2008 Society of Photo-Optical Instrumentation Engineers. One print or electronic copy may be made for personal use only. Systematic reproduction and distribution, duplication of any material in this paper for a fee or for commercial purposes, or modification of the content of the paper are prohibited.

**Citation format:** C. Soussen and J. Idier, “Reconstruction of three-dimensional localized objects from limited angle x-ray projections: an approach based on sparsity and multigrid image representation,” *Journal of Electronic Imaging*, vol. 17, no. 3, Aug. 2008

**DOI abstract link format:** <http://dx.doi.org/10.1117/1.2954960>

## **Reconstruction of three-dimensional localized objects from limited angle X-ray projections: an approach based on sparsity and multigrid image representation**

Charles Soussen

*Centre de Recherche en Automatique de Nancy*

*UMR 7039, Nancy-Université, CNRS*

*Boulevard des Aiguillettes, B.P. 239, F-54506 Vandœuvre-lès-Nancy, France*

*E-mail: Charles.Soussen@cran.uhp-nancy.fr*

Jérôme Idier

*Institut de Recherche en Communications et Cybernétique de Nantes*

*UMR CNRS 6597, BP 92101*

*1 rue de la Noë,*

*44321 Nantes Cedex 3, France.*

(Dated: Aug. 2008)

## Abstract

We report on three-dimensional image reconstruction from a limited set of computed tomography projections. We focus on configurations with very limited angle of view and on applications in which the image to be reconstructed is composed of one or several localized objects laying in a known background. We propose an original method based on the detection of the localized object voxels and on a sparse modeling of the image. Reconstruction is done by computing the maximum *a posteriori* estimator of the image parameters. To implement image reconstruction, we adopt a multigrid strategy in which coarse-to-fine resoled images are successively reconstructed. This strategy provides detection of localized object voxels as well as accurate initial solutions at each resolution level. Each optimization stage is carried out by using an iterative deterministic descent algorithm. We propose a convergent single-site update algorithm that consists of successive constrained optimizations with respect to one voxel at a time. We show the performance of the multigrid method on simulated data corresponding to a set of limited angle cone-beam projections of a synthetic image. The results are accurate, while both memory storage and numerical time of computation are dramatically reduced compared to the monogrid reconstruction method.

Keywords: X-ray tomography, 3D image reconstruction, anomaly detection and localization, anomaly reconstruction, positive image modeling, sparse image modeling, maximum *a posteriori* reconstruction, single-site update algorithm, multigrid reconstruction.

## I. INTRODUCTION

This paper deals with the tomographic reconstruction of a three-dimensional (3D) image composed of one or several localized objects laying in a known background. Such images are encountered in nondestructive evaluation (NDE) of materials and represent a volume that may contain anomalies (*e.g.*, air faults inside a metal). NDE is used for the online inspection of aerospace components, fuel rods, and steel pipes in nuclear power stations. In this context, several modalities are available, including eddy current, X-ray, or microwave imaging techniques [1–5]. The problem of image reconstruction from X-ray measurements is known to be a difficult problem, because the number and the angles of projection are often limited, due to the geometric constraints of the radiograph acquisition. In the case where the background is a known material, we can assume that the attenuation function inside the 3D volume reads  $f(x, y, z) = f_B(x, y, z) - f_L(x, y, z)$ , where  $f_B$  stands for the attenuation function of the background region (that is, the nonnegative attenuation function corresponding to a perfect, fault-free material), and  $f_L$  is an unknown function characterizing the presence of a localized fault at location  $(x, y, z)$ ,

$$f_L(x, y, z) \begin{cases} \neq 0 & \text{if } (x, y, z) \text{ lays inside the localized object area,} \\ = 0 & \text{otherwise.} \end{cases}$$

In the following, function  $f_L$  is chosen nonnegative. This choice is motivated by the NDE application, in which air and void faults are of negligible attenuation [ $f(x, y, z) = 0$ , hence  $f_L(x, y, z) = f_B(x, y, z) \geq 0$ ]. By a slight abuse of words, we will refer to the region where  $f_L(x, y, z) = 0$  as the **background area** (that is, the fault-free area), by contrast to the **localized object area**. The reconstruction problem aims at estimating the map of attenuation  $f(x, y, z)$  from the computed tomography (CT) measurements. Because  $f_B$  is known, the estimation of  $f_L(x, y, z)$  over the whole 3D volume affords both detection of localized objects and quantitative estimation of their position and size.

Voxel-based methods consist of discretizing the entire volume of interest into a set of voxels (*i.e.*, parallelepipedic volume elements) and then directly estimating the voxel values from the data. When the projection data are limited in number and/or in angles, the number of unknowns is often largely greater than the number of data. As the reconstruction of an acceptable image is not guaranteed, regularization is necessary. A classical choice is to model some prior information on the sought image and then use the Bayesian inference framework. Markov random fields utilizing intervoxel differences are a natural choice because they favor piecewise homogeneous images. The

attenuation image is then usually reconstructed in the maximum *a posteriori* (MAP) sense [6, 7].

In NDE applications, attenuation images are generally composed of a large number of background voxels, in comparison with the localized object voxels. Consequently, the attenuation image  $f_L(x, y, z)$  has many zero-valued voxels. One can then take account of this knowledge to regularize the reconstruction problem. A possible regularization is to restrict the image to be binary, hence reducing image reconstruction to the binary detection of the localized object voxels. Binary image reconstruction has been applied to vascular cross-sectional images in angiography [5, 8] and, more recently, to the NDE of materials [9]. However, binary reconstruction poses severe algorithmic difficulties, in terms of optimization of criteria over discrete domains. In order to afford a nonbinary reconstruction of the attenuation function, the use of a positive, continuous valued image model has been addressed, allowing annealing of the image values [10, 11]. A natural choice for such **positive prior distribution** is a Gamma distribution, or a mixture of independent Gamma distributions. Contrarily to Markov random fields, these priors are "pointwise" (*i.e.*, they do not take into account the interactions between neighboring voxels). The related distribution is parametrized by the variances of each Gamma distribution. In this paper, we consider at the same time the assumptions of piecewise homogeneity and positivity, following [12]. We utilize a Markov model defined from a combination of two types of energy functions: one involves neighboring voxels and favors image smoothness and the other applies to single voxels and draws their value towards zero. The computation of the MAP reconstruction image involves the optimization of an  $n$ -dimensional criterion under positivity constraints, where  $n$  stands for the number of voxels. We focus on convex criteria that can be optimized using deterministic descent algorithms. In particular, we distinguish classical descent algorithms that work on the whole set of parameters together [12] and single-site update strategies that involve successive optimizations with respect to one voxel at a time [13–15].

Despite their simplicity, voxel-based methods encounter limitations for high-resoluted images; when the volume is described by a large number of voxels, its reconstruction requires a large amount of memory space and is highly limited in speed of convergence. In contrast, alternative image models based on deformable contours have enjoyed considerable interest because they rely on a low number of parameters and do not need a volume discretization. This approach is well suited to describe compact objects [16–20], but it suffers from several restrictions. Actually, the attenuation function must be uniform inside the objects and the number of objects embedded inside the image has to be known as well. The use of implicit contours described by a level set

of a higher dimensional function can alleviate the latter limitation, as the number of objects is no longer needed [21]. Nevertheless, implicit representations of contours are computationally expensive because they require the computation and update of a full discrete image volume. The combination of both voxel and explicit contour-based models into a unified mixed approach has been investigated in the literature. This approach, which performs joint estimation of the localized object contours and the voxel values, yields promising results for the reconstruction of textured objects and background despite its relative complexity [22, 23].

Another natural, yet simple strategy to decrease the parametrization of the image volume is to detect a region of interest (ROI) inside the image in which the localized objects are embedded. One can thus generate an irregular image grid in which the voxels do not have the same size and/or shape and are distributed more densely in the vicinity of the ROI, that is in the regions containing significant details [24]. For an image composed of localized objects, several researchers have attempted to detect a ROI inside the image. A hypothesis testing approach has been used to detect the presence of uniform anomalies inside the volume from X-ray data, and to determine their position by using a multigrid framework [2, 25]. In [9], the image is assumed binary and a necessary condition for the reconstruction of background voxels is provided, based on marginal *a posteriori* probabilities. This test is very fast to compute, affording the predetection of a set of background voxels and thus the formation of a ROI embedding the localized objects. Computing a ROI prior to image reconstruction is advantageous since the image parametrization is dramatically reduced. One may also design a more highly resolved discretization of the volume inside the ROI, when the ROI domain is small.

In medical imaging, the reconstruction of the volume embedded inside a ROI from X-ray projections has been extensively studied. Wavelet image representations are very popular because they afford reconstruction of the interior of a ROI at a fine-resolution level and reconstruction of the rest of the image at a coarser level. These local tomography methods result in a drastic reduction of the radiation exposure delivered to the patient because the reconstruction can be done from the projection rays that intersect the ROI and from a sparse sampling of the projections away from the ROI [26–29]. Nevertheless, wavelet-based reconstructions rely on a complete set of projection angles. Setting aside the ROI reconstruction problem, multigrid algorithms, affording successive reconstruction of coarse-to-fine "complete" images, have enjoyed considerable success in CT applications because they yield more accurate reconstructions within a very limited time of computation. Basic multigrid implementations aim at reconstructing a sequence of coarse-to-

fine images and at using the reconstruction at a given grid level to compute the initial solution at the finer level [30, 31]. Multigrid models have been extended to nonlinear inverse problems (*e.g.*, diffusion optical tomography which involves the reconstruction of a positive image from nonlinear measurements) [6, 32–34]. The related multigrid algorithms are based on coarse-to-fine image updates and on fine-to-coarse updates as well, according to the so-called V-cycle scheme. The computation of the MAP reconstruction image at each resolution level requires a dynamical adjustment of the cost functions at different levels due to the nonlinearity of the inverse problem. In emission tomography, more elaborate Bayesian formulations relying on Markov random fields and on a multigrid pyramidal representation have also been investigated, allowing hyperparameter estimation at any resolution level using the reconstructed image at a coarser level [35, 36].

In this paper, we propose a method that performs the detection of the ROI embedding the localized objects in conjunction with the reconstruction of the localized object voxels. The image model relies on a sparse description of the volume  $f(x, y, z)$ , taking account of the localized object voxels only. This description is highly parsimonious because the localized object regions are generally of small size relative to the rest of the volume. Therefore, the sparse model permits an efficient exploration of the specific regions containing the localized objects. The detection of the ROI domain (or similarly, of the complementary set of background voxels) is a key problem. We propose a solution to this problem using a multigrid strategy, which affords successive reconstructions of coarse-to-fine positive images and recursive detection of the background voxels as well. At each level, positive image reconstruction will be carried out by using a single-site update (SSU) optimization algorithm with provable convergence.

The rest of the paper is organized as follows. Section II introduces the 3D image reconstruction problem. We specify the monogrid image discretization and parametrization in both complete and sparse cases. Then, we formulate the image reconstruction problem as an ill-posed inverse problem. In Section III, we develop the monogrid positive image reconstruction method, providing the MAP estimator of the complete image voxels. Regularization is composed of two terms related to both annealing and local homogeneity assumptions. To compute the MAP solution, we will discuss the choice of a deterministic descent algorithm and will propose an iterative SSU algorithm. Section IV provides an extension of this method to sparse image reconstruction. Localized object regions are detected using a multigrid strategy affording successive reconstruction of coarse-to-fine images. Finally, Section V exhibits numerical simulations performed on a set of limited angle projections of a synthetic 3D image formed of two small localized objects laying in

a uniform background and located together along the direction of the projection rays. We show the ability of the method to provide an accurate identification of the object locations as well as the discrimination between the two objects.

## II. PROBLEM STATEMENT

In Section I, we assumed that the attenuation function is of the form  $f(x, y, z) = f_B(x, y, z) - f_L(x, y, z)$ , where  $f_B$  is the known attenuation of the fault-free volume, and  $f_L$  is an unknown nonnegative function associated to the localized objects [ $f_L(x, y, z) \neq 0$  if and only if  $(x, y, z)$  lays inside the localized object area]. Under this assumption, the reconstruction problem consists of estimating the nonnegative image  $f_L(x, y, z)$  from a set of noisy projections of  $f$ . Because of the linearity of the X-ray projection operator, this problem is equivalent to the reconstruction of  $f_L$ , given its own projections, estimated up to the precomputation of the projections of  $f_B$ . In the following, we focus on the tomographic reconstruction of  $f_L$ , which will be renamed  $f$  for convenience. We refer to the region where  $f(x, y, z) = 0$  as the background area, by contrast to the localized object area.

In this section, we first introduce discrete parametrizations of the 3D attenuation image and then give a formulation of the direct model, relating the X-ray measurements to the image parameters. This formulation will allow us to solve the image reconstruction problem by directly estimating the image parameters from the data.

### A. Image discretization: complete and sparse parametrizations

The volume of interest is discretized into a set of  $n$  voxels of identical size, where the voxel denomination stands for the parallelepipedic volume element. The discrete attenuation image is then represented by vector  $\mathbf{f} = [f_1, \dots, f_n]^t \in \mathbb{R}_+^n$ . In the following, we refer to this parametrization as the **complete parametrization**.

Let us assume that we have a detection rule for the location of the background voxels ( $f_i = 0$ ). We denote by  $\mathcal{B} \subset \{1, \dots, n\}$  the set of the background voxel indexes, and by  $\mathcal{A} = \{1, \dots, n\} \setminus \mathcal{B}$  the complementary set of voxels. These voxels, referred to as **active voxels**, are candidates to belong to the localized object regions (*i.e.*,  $f_i > 0$ ). Active voxels are represented by a vector  $\mathbf{f}_a$ , extracted from the global image vector  $\mathbf{f}$ . Denoting by  $a$  the number of active voxels, and up to a

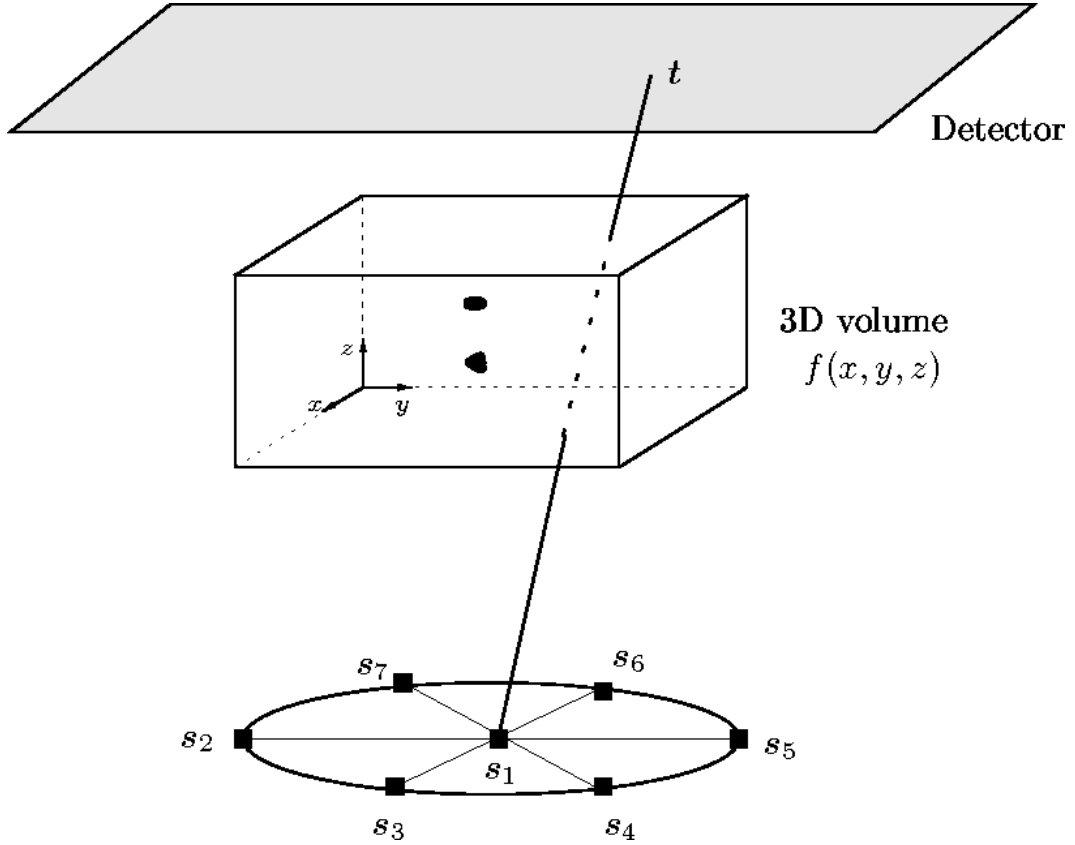


FIG. 1: Cone-beam projection parametrization. The volume of interest is represented by a parallelepipedic domain. A projection line  $(s, t)$  is formed by a source position  $s \in \mathbb{R}^3$  located below the volume of interest, and a detector position  $t \in \mathbb{R}^3$  laying on the horizontal detector plane, above the volume. All projections are defined with respect to the same horizontal plane. A radiograph image is obtained from a single source position  $s_k$  and a collection of X-ray projections  $p(s_k, t)$  onto the detector plane.

rearrangement of the voxels, the complete image parametrization rereads  $\mathbf{f} = [\mathbf{f}_a^t; \mathbf{0}^t]^t$ , where  $\mathbf{0}$  is the null vector of length  $n - a$ .

## B. Projection modeling

The X-ray projection operator computes the line projections of a given image  $f(x, y, z)$ ,

$$p(\mathbf{s}, \mathbf{t}) = \int_{(s,t)} f(x, y, z) dl,$$

where  $(\mathbf{s}, \mathbf{t})$  is the projection line passing through the source and the detector positions  $\mathbf{s}$  and  $\mathbf{t}$ , respectively; see Fig. 1.

Let us fix a source position  $\mathbf{s} = \mathbf{s}_k$  ( $k = 1, \dots, m$ ). The corresponding cone-beam projection of the volume is a two-dimensional radiograph image obtained by putting together the projection values  $p(\mathbf{s}_k, \mathbf{t})$  for  $n_{\mathbf{t}}$  discrete values of  $\mathbf{t}$  in the detector plane. This projection image is then represented by vector  $\mathbf{p}_k$  of size  $n_{\mathbf{t}} \times 1$ . Finally, the global projection vector yielded by all sources  $\mathbf{s}_k$  is the result of the concatenation of vectors  $\mathbf{p}_k$ :  $\mathbf{p} = [\mathbf{p}_1^t, \dots, \mathbf{p}_m^t]^t$ . This single vector represents the collection of all  $m$  radiograph images.

For images  $f(x, y, z)$  that are discretized into a set of voxels  $\mathbf{f} = [f_1, \dots, f_n]^t$ , the X-ray projection operator rereads  $\mathbf{p} = \mathbf{H}\mathbf{f}$ , where  $\mathbf{H}$  is a  $M \times n$  projection matrix, only depending on the geometry of X-ray projection acquisition.  $M = m n_{\mathbf{t}}$  stands for the global number of detector pixels, and  $n$  is the number of voxels.

For a sparse image modeling  $\{1, \dots, n\} = \mathcal{A} \cup \mathcal{B}$ , the projection model rereads  $\mathbf{p} = \mathbf{H}_a \mathbf{f}_a$ , where  $\mathbf{H}_a$  is the new projection matrix, of size  $M \times a$ . Matrix  $\mathbf{H}_a$  is extracted from  $\mathbf{H}$  by keeping only the columns  $i$  such that  $i \in \mathcal{A}$ .

### C. Direct and inverse problems

We model the X-ray data as the noisy projections  $\mathbf{d} = \mathbf{p} + \mathbf{n}$  of the sought image, where the noise  $\mathbf{n}$  takes account of both errors of projection modeling and measurement. Actually, there are many sources of error, including the photon counting errors, the electronic errors occurring while recording data with a CCD camera, the influence of the finite width of the projection beam as well as the diffusion of the X-rays along all spatial directions. Some of these phenomena can be easily modeled using probability density functions [37], but it is rather difficult to tackle all of them together without making any simplifying assumption.

Let us consider the photon counting errors alone. The Poisson model is the most appropriate to describe that the measurements are related to a counting process [9, 38]. According to Beer law, the noisy projections are related to the photon counts in the following way:

$$d(\mathbf{s}_k, \mathbf{t}) = -\log \left[ \frac{\tau(\mathbf{s}_k, \mathbf{t})}{\tau(\mathbf{s}_k)} \right],$$

where  $\tau(\mathbf{s}_k)$  is the photon emission rate of the  $k$ th source and  $\tau(\mathbf{s}_k, \mathbf{t})$  is the counting rate of the detector  $\mathbf{t}$ . The photon count  $\tau(\mathbf{s}_k, \mathbf{t})$  is then modeled by a Poisson distributed random variable with mean and variance  $\tau(\mathbf{s}_k) \exp(-p(\mathbf{s}_k, \mathbf{t}))$ . When the photon counting rates are high at each radiograph pixel and of same magnitude, which is often the case in NDE applications, it is possible

to use an independent identically distributed (i.i.d.) and Gaussian model  $\mathbf{d} = \mathbf{p} + \mathbf{n}$  instead of the Poisson model. Note that for low counting rates, the Poisson model can also be approximated in a precise manner by an additive and Gaussian distribution whose variance is not constant and depends on the projection measurements  $d(\mathbf{s}_k, \mathbf{t})$ , according to [38, 39].

In the following, we will assume that the noisy projections read:

$$\mathbf{d} = \mathbf{H}\mathbf{f} + \mathbf{n} = \mathbf{H}_a\mathbf{f}_a + \mathbf{n},$$

where the noise vector is additive, i.i.d. and Gaussian. Here, the Gaussian assumption is not the result of a statistical hypothesis on the observation errors. It is mainly chosen for simplicity reasons. The reconstruction method presented in this paper can be straightforwardly extended to the case where the variance of the Gaussian noise is not constant. It is well known that when the projections are limited in number and in angles, the inverse problem, which consists of estimating  $\mathbf{f}$  from the data  $\mathbf{d}$ , is very ill-posed [40]. In 3D problems, the number  $n$  of unknowns is generally greater than the number of data. To reduce the range of possible solutions and to obtain a realistic image, it is necessary to regularize the solution by introducing some prior assumptions on the sought image. In the following, we will enforce positivity of the voxel values and assume that a fair amount of voxels are zero valued. The latter assumption states that the background voxels usually are preponderant in the image. At the same time, piecewise smooth reconstructions will be favored, in which neighboring voxels tend to have homogeneous values.

### III. MONOGRID RECONSTRUCTION

#### A. MAP estimation of the attenuation image

In this section, we consider the complete modeling  $\mathbf{f} = [f_1, \dots, f_n]^t$  of the attenuation image. We perform voxel estimation in the MAP sense, by minimizing over  $\mathbb{R}_+^n$  a penalized cost function of the form,

$$\mathcal{J}(\mathbf{f}) = \|\mathbf{d} - \mathbf{H}\mathbf{f}\|^2 + \lambda\mathcal{D}(\mathbf{f}) + \mu \sum_{i=1}^n f_i, \quad (1)$$

where

$$\mathcal{D}(\mathbf{f}) = \sum_{i,j,i \sim j} \phi(f_i - f_j).$$

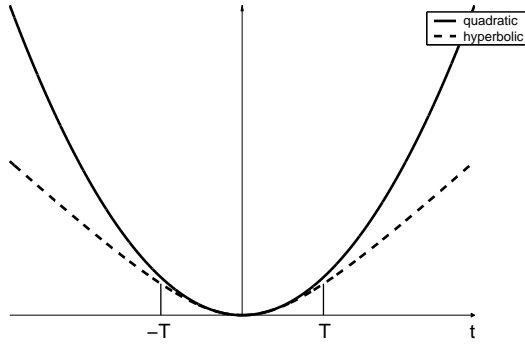


FIG. 2: Plot of the hyperbolic function  $\phi(t) = 2T \left( \sqrt{t^2 + T^2} - T \right)$ , together with the quadratic function  $t^2$ .  $\phi$  is quadratic at the origin and behaves as  $2T|t|$  when  $|t|$  is large.

In this formulation,  $\sim$  denotes the six-neighborhood relationship between voxels: voxels  $i$  and  $j$  are neighbors *if and only if* they share a common face.  $\phi : \mathbb{R} \rightarrow \mathbb{R}_+$  is a convex and even potential function, which is  $\mathcal{C}^1$  and increasing on  $\mathbb{R}_+$ .

The compound energy  $\mathcal{J}(\mathbf{f})$  is composed of a fidelity-to-data term and of two penalization terms, which favor piecewise homogeneous images and zero-valued voxels, respectively [12]. In order to favor the presence of sharp edges in the reconstructed image, function  $\phi$  is chosen quadratic at the origin and linear at infinity. We select the hyperbolic function (see Fig. 2) defined by

$$\phi(t) = 2T \left( \sqrt{t^2 + T^2} - T \right). \quad (2)$$

When  $T$  is large,  $\phi$  has a quadratic behavior and the regularization favors oversmoothed images, whereas for low values of  $T$ , sharp edges are more likely to appear. The second penalization term is equal to the sum of the voxel values. Because the minimization of  $\mathcal{J}$  is performed over  $\mathbb{R}_+^n$ , this term is minimal when all voxels are set to 0. Consequently, its role is to favor the detection of background voxels, whereas removing this term would allow free estimation of positive valued voxels.

### B. Optimization algorithm: single-site update strategy

**Proposition 1.** *For the  $\phi$  function defined in (2), criterion  $\mathcal{J}$  is a strictly convex function of  $\mathbf{f}$  on  $\mathbb{R}_+^n$  provided that  $\lambda > 0$  and that at least one projection ray intersects the volume of interest.*

Note that the latter condition is always true in practice.

*Proof.* Straightforwardly, criterion  $\mathcal{J}$  is convex on  $\mathbb{R}_+^n$  as a sum of convex terms. In addition, it can be shown that a criterion of the form

$$\|\mathbf{d} - \mathbf{H}\mathbf{f}\|^2 + \lambda \sum_{c=1}^C \phi(\mathbf{v}_c^t \mathbf{f}), \quad (3)$$

where  $\mathbf{v}_c$  are  $n \times 1$  vectors, is strictly convex on  $\mathbb{R}^n$  under the following conditions [41]:

- $\lambda > 0$  and  $\phi$  is strictly convex on  $\mathbb{R}$ ;
- $\text{Ker } \mathbf{H} \cap \text{Ker } \mathbf{V} = \{\mathbf{0}\}$ , where  $\text{Ker}(\cdot)$  denotes the null space of an operator and  $\mathbf{V}$  is the matrix of size  $C \times n$  whose rows are formed by vectors  $\mathbf{v}_1^t, \mathbf{v}_2^t, \dots, \mathbf{v}_C^t$ .

Let us apply this result to the criterion  $\mathcal{J}$  defined in (1). In the case where  $\mu = 0$ ,  $\mathcal{J}(\mathbf{f})$  rereads (3), where  $\phi$  is strictly convex and vectors  $\mathbf{v}_c$  are replaced by the vectors  $\mathbf{w}_{ij}$ , defined such that  $\mathbf{w}_{ij}^t \mathbf{f}$  are the finite differences  $f_i - f_j$  involved in the sum  $\mathcal{D}(\mathbf{f})$ . One can easily check that:

- $\text{Ker } \mathbf{V}$  is the set of constant images, thus  $\text{Ker } \mathbf{H} \cap \text{Ker } \mathbf{V}$  is the set of constant images whose projection is equal to  $\mathbf{0}$ ;
- the projection  $\mathbf{H}\mathbf{f}$  of a constant image is equal to  $\mathbf{0}$  *if and only if*  $\mathbf{f} = \mathbf{0}$ . The reason is that the elements of  $\mathbf{H}$  are all nonnegative and that  $\mathbf{H} \neq \mathbf{0}$ , since at least one projection ray intersects the volume of interest. As all the voxels share the same value,  $\mathbf{H}\mathbf{f} = \mathbf{0}$  only when  $\mathbf{f} = \mathbf{0}$ .

As a consequence, criterion  $\|\mathbf{d} - \mathbf{H}\mathbf{f}\|^2 + \lambda \mathcal{D}(\mathbf{f})$  is strictly convex on  $\mathbb{R}^n$  and thus on  $\mathbb{R}_+^n$ . In the case where  $\mu \neq 0$ ,  $\mathcal{J}$  is strictly convex as the sum of convex and strictly convex terms.  $\square$

Since  $\mathbb{R}_+^n$  is a convex set, the strict convexity of  $\mathcal{J}$  implies that  $\mathcal{J}$  has a unique global minimizer on  $\mathbb{R}_+^n$  which can be obtained using an iterative local optimization algorithm. In [42], we chose the projected gradient algorithm, which is a constrained analog of the classical gradient descent algorithm [43]. However, this algorithm is known to be very slow. Following [13], here we rather choose an SSU strategy, which consists of successive minimizations of the criterion with respect to one voxel at a time. However, the scalar subproblem of minimizing  $\mathcal{J}$  with respect to a single voxel  $f_i$  admits no closed-form solution. Resorting to a half-quadratic formulation of the optimization problem [44, 45] provides an elegant solution with provable convergence.

Let us consider Geman and Reynolds's augmented criterion

$$\mathcal{K}(\mathbf{f}, \mathbf{b}) = \|\mathbf{d} - \mathbf{H}\mathbf{f}\|^2 + \lambda \tilde{\mathcal{D}}(\mathbf{f}, \mathbf{b}) + \mu \sum_{i=1}^n f_i,$$

where  $\tilde{\mathcal{D}}(\mathbf{f}, \mathbf{b}) = \sum_{i \sim j} [b_{ij}(f_i - f_j)^2 + \psi(b_{ij})]$ , and the auxiliary function  $\psi$  is defined as the opposite of the concave conjugate of  $\phi(\sqrt{\cdot})$  [46]. Because  $\phi(\sqrt{\cdot})$  is concave, it is, in turn, the concave conjugate of  $-\psi$ , and functions  $\psi$  and  $\phi$  satisfy

$$\begin{aligned}\psi(b) &= -\min_{f \in \mathbb{R}} (bf^2 - \phi(f)), \\ \phi(f) &= \min_{b > 0} (bf^2 + \psi(b)).\end{aligned}\quad (4)$$

The augmented criterion depends on the original vector  $\mathbf{f}$ , but also on a set of auxiliary variables  $\mathbf{b} = \{b_{ij} > 0, i \sim j\}$ . From the definition (4) of  $\psi$ , it follows that:

$$(\hat{\mathbf{f}}, \hat{\mathbf{b}}) = \arg \min_{\mathbf{f} \in \mathbb{R}_+^n, \mathbf{b}} \mathcal{K}, \quad (5)$$

where  $\hat{\mathbf{f}}$  is defined as the minimizer of  $\mathcal{J}$  over  $\mathbb{R}_+^n$ . As a consequence, the minimization of  $\mathcal{K}$  with respect to  $(\mathbf{f}, \mathbf{b})$  provides an indirect means to minimize  $\mathcal{J}$ .

In [45], it is shown that under the following hypotheses:

1.  $\phi$  is convex on  $\mathbb{R}$ ,
2.  $\phi$  is even,
3.  $\phi(\sqrt{\cdot})$  is concave on  $\mathbb{R}_+$ ,

criterion  $\mathcal{K}$  is convex in  $(\mathbf{f}, \mathbf{b})$ . Clearly, the hyperbolic function  $\phi$  defined by (2) fulfills the above conditions. The convexity of  $\mathcal{K}$  guarantees that a local descent algorithm provides the global minimizer of  $\mathcal{K}$  and thus the minimizer of  $\mathcal{J}$ . In particular, the SSU algorithm, which performs successive updates of scalar variables  $f_i$  and  $b_{ij}$ , is well suited to solve (5), as  $\mathcal{K}$  is quadratic in  $\mathbf{f}$  and the dependence of  $\mathcal{K}$  with respect to  $\mathbf{b}$  reduces to the separable term  $\sum_{i \sim j} \psi(b_{ij})$ , in which the auxiliary variables are decoupled. In other words, the scalar subproblem of minimizing  $\mathcal{K}$  with respect to a single voxel  $f_i$  or a single auxiliary variable  $b_{ij}$  can be straightforwardly solved. We refer the reader to [45] for a detailed study of convergence of the SSU algorithm for minimization of Geman and Reynolds's augmented criterion.

Formally, the optimization of  $\mathcal{K}$  with respect to a single voxel  $f_i$  reads

$$f_i = \max \left\{ 0, f_i + \frac{[\mathbf{H}^t \mathbf{d}]_i - [\mathbf{H}^t \mathbf{H} \mathbf{f}]_i + \lambda \sum_{j \sim i} b_{ij} (f_j - f_i) - \mu/2}{[\mathbf{H}^t \mathbf{H}]_{ii} + \lambda \sum_{j \sim i} b_{ij}} \right\}, \quad (6)$$

TABLE I: SSU reconstruction algorithm for monogrid image reconstruction.

---



---

Set initial solution  $\mathbf{f}(0)$ .

---

For  $k = 1, \dots, K$ ,

**[Basic SSU loop]**

For all voxel  $i \in \{1, \dots, n\}$ ,

**[Perform optimization of  $\mathcal{K}(\mathbf{f}, \mathbf{b})$  with respect to single voxel  $f_i$ ]**

Update  $f_i$  using (6), in which variables  $b_{ij}$  are computed using (7).

End For.

Set  $\mathbf{f}(k) = \{f_1, \dots, f_n\}$ .

End For.

---



---

and the optimization of  $\mathcal{K}$  with respect to a single auxiliary variable  $b_{ij}$  leads to the simple calculation

$$b_{ij} = \begin{cases} \frac{\phi'(f_i - f_j)}{2(f_i - f_j)} & \text{if } f_i \neq f_j, \\ 1 & \text{otherwise.} \end{cases} \quad (7)$$

The latter result is a basic result of the duality theory [45]. Here, let us stress that the knowledge of  $\psi$  is not necessary to compute (6) and (7). A more detailed description of the SSU algorithm can be found in [14, 15] in the case of image deblurring. Our algorithm is a simple extension of Brette and Idier’s algorithm [14] to the image reconstruction problem, including positivity constraints.

### C. Implementation of the SSU algorithm

The SSU algorithm is finally summarized in Table I. In the following paragraphs, we discuss the main difficulties of the implementation, namely, the storage and the recomputation of large data arrays. Finally, we will discuss the choice of the parameters involved in the monogrid reconstruction method (initial solution, hyperparameters).

### 1. Data structure for storage of image and projection matrices

The implementation of the SSU algorithm raises several algorithmic difficulties, as the projection matrix  $\mathbf{H}$ , of size  $M \times n$ , is of enormous dimensions. Typical values of  $M$  and  $n$  can reach  $10^4$  to  $10^6$  depending on the number of projections and the desired resolution of the reconstructed image (see Section V). Although  $\mathbf{H}$  is sparse, the number of matrix elements, which are not equal to zero, remains huge, which makes it not possible to store  $\mathbf{H}$  on a workstation, even in a sparse description. Similarly, matrix  $\mathbf{H}^t\mathbf{H}$ , of size  $n \times n$ , cannot be stored and its computation would be burdensome. In the following, we propose a data structure that avoids the memory storage of huge arrays and, based on this structure, we derive an algorithm that restricts the number of recomputations of the matrix elements  $H_{ki}$  for each radiograph pixel  $k$  and for each image voxel  $i$ . The recomputation of  $H_{ki}$  is numerically expensive when performed many times, because it requires one to compute the length of the intersection between a line (the projection ray) and a parallelepipedic volume (the voxel).

Our data structure relies on four buffer arrays:

- `buff_backproj`, of size  $n$ . Stores the data backprojection  $\mathbf{H}^t\mathbf{d}$ .
- `buff_HtH`, of size  $n$ . Stores the diagonal elements of matrix  $\mathbf{H}^t\mathbf{H}$ :  $[\mathbf{H}^t\mathbf{H}]_{ii} = \sum_k H_{ki}^2$ .
- `buff_p`, of size  $M$ . Stores the projection vector  $\mathbf{p} = \mathbf{H}\mathbf{f}$ .
- `buff_Hi`, of size  $M$ . Stores the current column of matrix  $\mathbf{H}$ . We also denote this column vector by  $\mathbf{H}_{\bullet i}$ . It is formed of the collection of all values  $\{H_{ki}, k = 1, \dots, M\}$ .

The first two buffers are computed prior to any SSU of voxels; their content remains unchanged during the SSU iterations. The other two are recomputed for each voxel update. `buff_Hi` is entirely recomputed when a new voxel is visited, whereas `buff_p` is updated with a limited computation cost.

*a. Update of a voxel* The update of the  $i$ th voxel relies on the implementation of (6). It is based on a direct combination of the four buffers, and does not necessitate the storage of the auxiliary variables  $b_{ij}$ ,

- compute buffer `buff_Hi`,
- compute  $[\mathbf{H}^t\mathbf{H}\mathbf{f}]_i = [\mathbf{H}^t\mathbf{p}]_i = \sum_k H_{ki}p_k$  using `buff_Hi` and `buff_p`,

- directly compute  $\sum_{j \sim i} b_{ij}(f_j - f_i)$  and  $\sum_{j \sim i} b_{ij}$  using (7),
- apply (6) to update  $f_i$ .

*b. Update of projections* When the  $i$ th voxel is updated, let us denote by  $f_i$  and  $f'_i$  its former and new values, where  $f'_i$  is computed using (6). Denoting  $\delta f_i = f'_i - f_i$ , the new image vector reads  $\mathbf{f}' = \mathbf{f} + \delta \mathbf{f}$ , where  $\delta \mathbf{f} = [0, \dots, 0, \delta f_i, 0, \dots, 0]^t$ . Hence, the new projection vector reads

$$\mathbf{p}' = \mathbf{H} \mathbf{f}' = \mathbf{p} + \delta \mathbf{p}, \quad \text{where } \delta \mathbf{p} = \mathbf{H} \delta \mathbf{f} = \delta f_i \mathbf{H}_{\bullet i}. \quad (8)$$

As vector  $\mathbf{H}_{\bullet i}$  is stored in buffer `buff_Hi`, the update of  $\mathbf{p}$  is straightforward and does not necessitate any other computation.

*c. Memory storage and computation cost* The overall memory storage of the SSU algorithm amounts to  $2M+3n$  scalar elements related to the four buffers and the image vector  $\mathbf{f}$ . This storage is largely inferior to the size of matrices  $\mathbf{H}$  and  $\mathbf{H}^t \mathbf{H}$ .

When a voxel  $i$  is updated, the corresponding column  $\mathbf{H}_{\bullet i}$  is recomputed. During an SSU iteration, this computation cost is then equivalent to one single computation of  $\mathbf{H}$ . Similarly, when a voxel  $i$  is updated, the recomputation of  $[\mathbf{H}^t \mathbf{H} \mathbf{f}]_i = [\mathbf{H}^t \mathbf{p}]_i$  amounts to one dot product between vectors  $\mathbf{p}$  and  $\mathbf{H}_{\bullet i}$ , which are already stored. The cost of computation of all terms  $[\mathbf{H}^t \mathbf{H} \mathbf{f}]_i$  during an SSU iteration is then equivalent to one matrix-vector product ( $\mathbf{H}^t \mathbf{p}$ ), where the matrix and the vector are both already stored.

In conclusion, when  $\mathbf{H}$  cannot be stored because of its size, one iteration of the SSU algorithm requires only one computation of  $\mathbf{H}$ , and other matrix and scalar computations. This cost is very limited in comparison to other algorithms that work on  $\mathcal{J}(\mathbf{f})$  and on all the voxels together. For the steepest descent algorithm, each iteration requires one backprojection computation ( $\mathbf{H}^t \mathbf{p}$ ) to compute  $\nabla \mathcal{J}(\mathbf{f})$  and several projection computations ( $\mathbf{H} \mathbf{f}$ ) to compute  $\mathcal{J}(\mathbf{f})$  during the line-search procedure.

The detailed implementation of the SSU algorithm with limited memory storage is finally summarized in Table II.

## 2. Practical settings of optimization parameters

In practice, we compute the data backprojection  $\mathbf{H}^t \mathbf{d}$  in order to provide the initial solution  $\mathbf{f}(0)$ . The maximum number of iterations is fixed relative to the number of voxels and we termi-

TABLE II: SSU algorithm: implementation and memory storage.

---



---

Compute and store buffer arrays `buff_backproj` and `buff_HtH`, of size  $n$ .

Set the initial solution  $\mathbf{f}$  to be the data backprojection (`buff_backproj`).

Compute  $\mathbf{p} = \mathbf{H}\mathbf{f}$ , and store the result in `buff_p`.

For  $k = 1, \dots, K$ , **[SSU loops]**

For all voxel  $i \in \{1, \dots, n\}$ ,

Compute buffer `buff_Hi`, representing the column vector  $\mathbf{H}_{\bullet i}$ .

Compute  $[\mathbf{H}^t \mathbf{H} \mathbf{f}]_i$  by using `buff_Hi` and `buff_p`.

Update voxel  $f_i$  by using (6), in which  $b_{ij}$  are directly computed using (7).

Update projection vector  $\mathbf{p}$  by using (8) and buffer `buff_Hi`.

End For.

End For.

---



---

nate the descent algorithm if  $\mathcal{J}[\mathbf{f}(k)] - \mathcal{J}[\mathbf{f}(k+1)] < \varepsilon$  for some arbitrary threshold  $\varepsilon$ . Hyperparameters  $\lambda$ ,  $\mu$ , and  $T$  are selected empirically. Generally, we first set  $\lambda = 0$  and then assign a value to  $\mu$  by performing a few executions of the descent algorithm. This setting favors annealing of the background voxels. If necessary, a similar setting of  $\lambda$  can be done in order to preserve the image smoothness. Parameter  $T$  is set relative to the range of attenuation values (e.g.,  $T = 0.01$  when the image values are expected to vary between 0 and 1). However, a low value of  $T$  tends to reduce the speed of convergence of the algorithm, as function  $\phi$  and, hence, criterion  $\mathcal{J}$  become almost nondifferentiable.

#### IV. SPARSE AND MULTIGRID IMAGE RECONSTRUCTION

In this section, we design an original reconstruction method that offers significant reduction of the image parametrization in conjunction with the detection of background voxels. The joint detection and reconstruction method relies on the combination of the sparse image model introduced in Section II with a multigrid strategy.

### A. Sparse image reconstruction

We first assume that we have a detection rule for the location of active and background voxels. Given this segmentation  $(\mathcal{A}, \mathcal{B})$  of the set of voxels, the discrete image is now parametrized by the active voxels  $\mathbf{f}_a$  belonging to  $\mathcal{A}$ , and up to a rearrangement of the voxels, we have  $\mathbf{f} = [\mathbf{f}_a^t, \mathbf{0}^t]^t$ . Sparse image reconstruction then reduces to the constrained minimization of the cost function  $\mathcal{J}(\mathbf{f}) = \mathcal{J}(\mathbf{f}_a; \mathbf{0})$  with respect to  $\mathbf{f}_a \in \mathbb{R}_+^a$ . Criterion  $\mathcal{J}$  rereads

$$\mathcal{J}(\mathbf{f}_a; \mathbf{0}) = \|\mathbf{d} - \mathbf{H}_a \mathbf{f}_a\|^2 + \lambda \mathcal{D}(\mathbf{f}_a; \mathbf{0}) + \mu \sum_{i=1}^a f_i,$$

where

$$\mathcal{D}(\mathbf{f}_a; \mathbf{0}) = \mathcal{D}(\mathbf{f}) = \sum_{\substack{j \in \{1, \dots, n\} \\ i \in \mathcal{A}, i \sim j}} \phi(f_i - f_j).$$

As criterion  $\mathcal{J}$  is strictly convex on  $\mathbb{R}_+^n$ , its restriction  $\mathcal{J}(\mathbf{f}_a; \mathbf{0})$  over  $\mathbb{R}_+^a$  is also strictly convex. Therefore, the constrained optimization of the latter criterion over  $\mathbb{R}_+^a$  can be carried out by the SSU algorithm to compute the minimizer  $\hat{\mathbf{f}}_a$ . In the same way as in Section III B, we define the Geman and Reynolds's augmented criterion by

$$\mathcal{K}(\mathbf{f}_a, \mathbf{b}) = \|\mathbf{d} - \mathbf{H}_a \mathbf{f}_a\|^2 + \lambda \tilde{\mathcal{D}}(\mathbf{f}_a, \mathbf{b}) + \mu \sum_{i=1}^a f_i,$$

where  $\tilde{\mathcal{D}}(\mathbf{f}_a, \mathbf{b}) = \sum_{i \sim j} [b_{ij}(f_i - f_j)^2 + \psi(b_{ij})]$  takes account of the neighboring voxels  $(i, j)$  such that  $i \in \mathcal{A}$  and  $j \in \{1, \dots, n\}$ . The minimization of  $\mathcal{K}$  with respect to  $f_i$  and  $b_{ij}$  reads (6) and (7), respectively. In these equations,  $f_j$  has to be replaced by 0 in cases where voxel  $j$  is not active. The algorithm presented in Table II is still valid for the implementation of fast SSU.

In the following, the sparse image representation will be denoted by  $\{\mathbf{f}_a, \mathcal{A}, \mathcal{B}\}$  or simply by  $\mathbf{f}_a$  when no ambiguity is possible. We will distinguish the SSU iterates  $\mathbf{f}_a(k)$  from the final image reconstruction  $\hat{\mathbf{f}}_a = \mathbf{f}_a(K)$  resulting from the SSU algorithm.

### B. Multigrid strategy

An essential prerequisite for the reduction of the image parametrization is the detection of the background voxels. In Section III, we designed our monogrid reconstruction method in order to favor background voxel detection. We now take advantage of this voxel detection and perform sparse image reconstruction using a multigrid strategy. Multigrid image reconstruction consists of

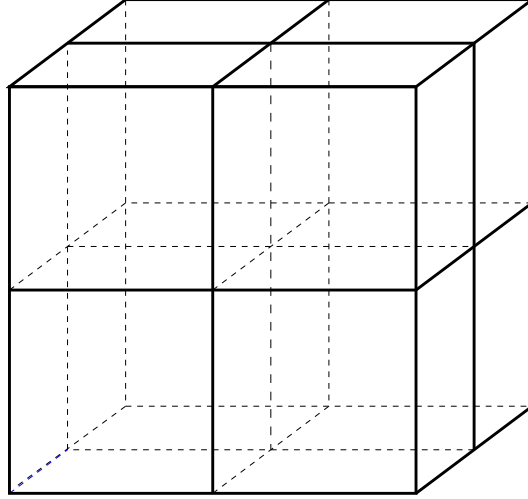


FIG. 3: Change of resolution: partition of a voxel into eight subvoxels.

- sequential reconstruction of sparse coarse-to-fine resolved images  $\hat{\mathbf{f}}^{(1)}, \hat{\mathbf{f}}^{(2)}, \dots, \hat{\mathbf{f}}^{(R)}$ .
- determination, at each resolution level  $r$ , of the image segmentation  $(\mathcal{A}_{r+1}, \mathcal{B}_{r+1})$  at the next finer resolution level  $r + 1$  given the current sparse reconstruction  $(\hat{\mathbf{f}}^{(r)}, \mathcal{A}_r, \mathcal{B}_r)$ .

In the following, we will denote by  $a_r = \#\mathcal{A}_r$  the number of active voxels at resolution level  $r$ . We now specify each step of the multigrid reconstruction scheme.

### 1. Multigrid image modeling

The coarsest image  $\mathbf{f}^{(1)}$  is a complete parametrization of the volume ( $a_1 = n$  voxels,  $\mathcal{A}_1 = \{1, \dots, n\}$  and  $\mathcal{B}_1 = \emptyset$ ) whereas finer images  $\mathbf{f}^{(2)}, \dots, \mathbf{f}^{(R)}$  are sparse. These images are obtained by discretizing the volume of interest on grids of  $8n, 8^2n, \dots, 8^{R-1}n$  voxels respectively, as each voxel is subdivided into eight subvoxels from one resolution to the next finer resolution; see Fig. 3.

### 2. Detection of background voxels

At a given resolution level  $r < R$ , let us assume that the image estimate  $(\hat{\mathbf{f}}^{(r)}, \mathcal{A}_r, \mathcal{B}_r)$  has been computed, where complementary sets  $\mathcal{A}_r$  and  $\mathcal{B}_r$  form a segmentation of the set of voxel indexes  $\{1, 2, \dots, 8^{r-1}n\}$ . At level  $r + 1$ , we define  $\mathcal{A}_{r+1}$  and  $\mathcal{B}_{r+1}$  as follows:

- enumerate the zero-valued voxels at level  $r$ :  $\tilde{\mathcal{B}}_r = \mathcal{B}_r \cup \{j \in \mathcal{A}_r, \hat{f}_j^{(r)} = 0\}$ ,

- define  $\mathcal{B}_{r+1}$  by subdividing all voxels of  $\widetilde{\mathcal{B}}_r$  into eight subvoxels,
- define  $\mathcal{A}_{r+1}$  by subdividing all positive voxels of  $\mathcal{A}_r$  into eight subvoxels.

### 3. Interpolation and initial condition

The initial estimate  $\mathbf{f}^{(r+1)}(0)$  at level  $r + 1$  is computed using the zero-order interpolation of image  $\widehat{\mathbf{f}}^{(r)}$  on the next finer grid. Given an active voxel  $i \in \mathcal{A}_r$ , this interpolation assigns the voxel value  $\widehat{f}_i^{(r)}$  to the eight subvoxels of  $i$ . This simple rule ensures continuity between both consecutive images: images  $\{\widehat{\mathbf{f}}^{(r)}, \mathcal{A}_r, \mathcal{B}_r\}$  and  $\{\mathbf{f}^{(r+1)}(0), \mathcal{A}_{r+1}, \mathcal{B}_{r+1}\}$ , although sampled upon two consecutive grids are identical representations of the volume.

### 4. Projection matrices

Let us denote by  $\mathbf{H}^{(r)}$  the projection matrix at level  $r$ .  $\mathbf{H}^{(r)}$  is a matrix of size  $M \times a_r$ , whose  $(k, i)$ th element is equal to the length of the intersection between the  $k$ th projection ray and the  $i$ th active voxel. At the next finer resolution level,  $\mathbf{H}^{(r+1)}$  is of size  $M \times a_{r+1}$ , and by construction of  $\mathbf{f}^{(r+1)}(0)$ , it follows that  $\mathbf{H}^{(r+1)} \mathbf{f}^{(r+1)}(0) = \mathbf{H}^{(r)} \widehat{\mathbf{f}}^{(r)}$ .

### 5. Optimization scheme

Multigrid image reconstruction involves sequential minimization of  $R$  criteria,

$$\widehat{\mathbf{f}}^{(r)} = \arg \min_{\mathbf{f}^{(r)} \in \mathbb{R}_+^{a_r}} \left\{ \mathcal{J}_r[\mathbf{f}^{(r)}] = \mathcal{J}(\mathbf{f}^{(r)}; \mathbf{0}) \right\}$$

given the initial estimate  $\mathbf{f}^{(r)}(0)$ . For the sake of simplicity, the dependence of  $\mathcal{J}_r$  on  $\{\mathcal{A}_r, \mathcal{B}_r\}$  is implicit as well as the rearrangement  $(\mathbf{f}^{(r)}; \mathbf{0})$  of the  $8^{r-1}n$  voxels. Here, criterion  $\mathcal{J}$  is associated with the complete parametrization at level  $r$ .

For all resolution levels, optimization is carried out using the local SSU algorithm described in Section III and extended in Section IV A to sparse image reconstruction. Observe that the image parametrization is complete at the coarsest resolution level ( $r = 1$ ), hence, reducing the optimization scheme to the monogrid reconstruction algorithm.

## 6. Hyperparameter setting

For all resolution levels, hyperparameters  $\lambda_r, \mu_r, T_r$  are selected recursively in order to satisfy

$$\forall r \in \{1, \dots, R-1\}, \mathcal{J}_{r+1}[\mathbf{f}^{(r+1)}(0)] = \mathcal{J}_r[\widehat{\mathbf{f}}^{(r)}]. \quad (9)$$

This condition states that images  $\widehat{\mathbf{f}}^{(r)}$  and  $\mathbf{f}^{(r+1)}(0)$  yield the same cost as they are identical representations of the volume.

**Proposition 2.** *The condition*

$$\lambda_{r+1} = \lambda_r/4, \quad \mu_{r+1} = \mu_r/8, \quad T_{r+1} = T_r. \quad (10)$$

*is sufficient to guarantee (9).*

*Proof.* By construction of  $\mathbf{f}^{(r+1)}(0)$ , each voxel of  $(\widehat{\mathbf{f}}^{(r)}, \mathcal{A}_r, \mathcal{B}_r)$  is subdivided into eight subvoxels of same value. The smoothness term of  $\mathcal{J}_{r+1}[\mathbf{f}^{(r+1)}(0)]$  is thus equal to four times that of  $\mathcal{J}_r[\widehat{\mathbf{f}}^{(r)}]$ , while the annealing term of  $\mathcal{J}_{r+1}[\mathbf{f}^{(r+1)}(0)]$  is equal to eight times that of  $\mathcal{J}_r[\widehat{\mathbf{f}}^{(r)}]$ . As the data-fidelity term is unchanged, (10) is a sufficient condition for (9).  $\square$

From Proposition 2, it follows that  $\lambda_r = \lambda_1/4^{r-1}$ ,  $\mu_r = \mu_1/8^{r-1}$ , and  $T_r = T_1$  for all  $r = 2, \dots, R$ . Hyperparameters can thus be easily computed at any level given their value at either the coarsest or the finest level.

**Remark 1.** *Let us denote by  $\mathcal{J}$  the criterion associated with the complete parametrization at the finest resolution level  $R$ , and by  $\mathbf{I}_r^R$  the zero-order interpolation operator, which maps an image  $\{\mathbf{f}^{(r)}; \mathbf{0}\}$  at level  $r$  onto an image  $\{\mathbf{f}^{(R)}; \mathbf{0}\}$  at the finest level  $R$ . Condition (9) guarantees the decrease of the sequence of reconstructed images  $\{\widehat{\mathbf{f}}^{(r)}, \mathcal{A}_r, \mathcal{B}_r\}$  in the sense of criterion  $\mathcal{J}$ ,*

$$\mathcal{J}(\widehat{\mathbf{f}}^{(R)}; \mathbf{0}) \leq \mathcal{J}[\mathbf{I}_{R-1}^R(\widehat{\mathbf{f}}^{(R-1)}; \mathbf{0})] \leq \dots \leq \mathcal{J}[\mathbf{I}_1^R(\widehat{\mathbf{f}}^{(1)}; \emptyset)].$$

*In other words, the solution  $\widehat{\mathbf{f}}^{(R)}$  obtained at the finest level is more accurate than the zero-order interpolation of any coarser level solution.*

The overall multigrid reconstruction algorithm is summarized in Table III.

TABLE III: Multigrid algorithm for sparse image reconstruction.

---



---

Perform backprojection  $\mathbf{f}^{(1)}(0)$  of the data  $\mathbf{d}$  on a grid of  $n$  voxels.

Set  $\mathcal{A}_1 = \{1, \dots, n\}$ ,  $\mathcal{B}_1 = \emptyset$ , and  $a_1 = n$  (all voxels are active).

Input  $\lambda_1, \mu_1, T$ .

---

For  $r = 1, \dots, R$ ,

Compute  $\widehat{\mathbf{f}}^{(r)} = \arg \min_{\mathbf{f}^{(r)} \in \mathbb{R}_+^{a_r}} \mathcal{J}_r[\mathbf{f}^{(r)}]$  from  $\mathbf{f}^{(r)}(0)$ .

If  $r < R$ ,

Define  $\mathcal{A}_{r+1}$  by sampling each nonnull voxel of  $\widehat{\mathbf{f}}^{(r)}$  into eight subvoxels.

Define  $\mathcal{B}_{r+1}$  by sampling all voxels of  $\mathcal{B}_r$  and all null voxels of  $\widehat{\mathbf{f}}^{(r)}$  into eight subvoxels.

Set  $a_{r+1} = \#\mathcal{A}_{r+1}$ .

Set  $\lambda_{r+1} = \lambda_r/4$ ,  $\mu_{r+1} = \mu_r/8$ .

Compute  $\mathbf{f}^{(r+1)}(0)$  using zero-order interpolation of  $\widehat{\mathbf{f}}^{(r)}$ .

End If.

End For.

---



---

## V. SIMULATION RESULTS

### A. Data simulation

The following simulation involves  $m = 7$  limited angle projections of a binary synthetic image, designed according to the geometry of Fig. 1. The synthetic image is composed of two localized spherical objects laying in a uniform background. The unknown attenuation function is thus defined by

$$f^*(x, y, z) = \begin{cases} 1 & \text{if } (x, y, z) \text{ lays inside one of the two spherical objects,} \\ 0 & \text{otherwise.} \end{cases}$$

The volume of interest is the cube  $(x, y, z) \in [0, 1]^3$ , and both spherical objects are of same size and are located along the vertical direction. Their center locations are  $(0.5, 0.5, 0.5)$  and

TABLE IV: Location of the seven X-ray sources. All sources  $\mathbf{s}_k = (x_k, y_k, z_k)$  are located inside the horizontal plane ( $z = -13$ ) and around central location  $\mathbf{s}_1 = (0.5, 0.5, -13)$ . Sources  $\mathbf{s}_2, \dots, \mathbf{s}_7$  lay on a circle of center  $\mathbf{s}_1$  and of radius equal to 3.75. Projection angles  $\theta_k$  are defined as the angles between the vertical direction  $(0, 0, 1)$  and the vector formed by  $\mathbf{s}_k$  and the average locations  $(0.5, 0.5, 1)$  in the detector plane. Projection angles are roughly equal to  $\pi/4$ .

$k$	1	2	3	4	5	6	7
$x_k$	0.50	0.50	-2.75	-2.75	0.50	3.75	3.75
$y_k$	0.50	-3.25	-1.38	2.38	4.25	2.38	-1.38
$\theta_k$	0	0.79	0.79	0.79	0.79	0.79	0.79

$(0.5, 0.5, 0.69)$ , respectively, and their radius is equal to 0.031; see Fig. 4 (a). The projection geometry is defined as follows. The seven sources  $\mathbf{s}_k = (x_k, y_k, z_k)$  are all located inside the horizontal plane ( $z = -13$ ) and around central location  $\mathbf{s}_1 = (0.5, 0.5, -13)$ . All six other sources lay on a circle of center  $\mathbf{s}_1$  and of radius equal to 3.75, according to the geometry of Fig. 1. Table IV displays the exact values of the source coordinates. The cone-beam projections are all computed on a same horizontal plane of equation ( $z = 1$ ). This plane is discretized by a set of  $128 \times 128$  square pixels partitioning the rectangular domain  $\{(x, y) \in [-0.30, 1.11] \times [-0.30, 1.11]\}$ . The simulated data are generated by computing the **exact** line projections[52] of analogic image  $f^*(x, y, z)$  and by adding an i.i.d. Gaussian noise to the projections. The signal to noise ratio is defined by  $\text{SNR} = 10 \log v_p/v_n$ , where  $v_p$  is the spatial variance of the projection signal and  $v_n$  is the ensemble variance of the noise. It is set to  $-10$  dB. The seven simulated radiographs are displayed in Fig. 4 (b).

The difficulty of the image reconstruction problem lies in the limited nature of the data. Specifically, all projection rays are close to the vertical direction hence complicating the discrimination of objects that are vertically aligned. The synthetic image of Fig. 4 (a) has been chosen in order to evaluate the capability of the reconstruction method to discriminate two close tiny objects, in a difficult case where the radiograph images do not qualitatively provide a clear discrimination between the two. In a more classical geometry of acquisition with a limited number of projections but with equidistributed angles, it is generally possible to localize the objects in a qualitative fashion using standard algorithms (*e.g.*, filtered backprojection). In the following, we evaluate both

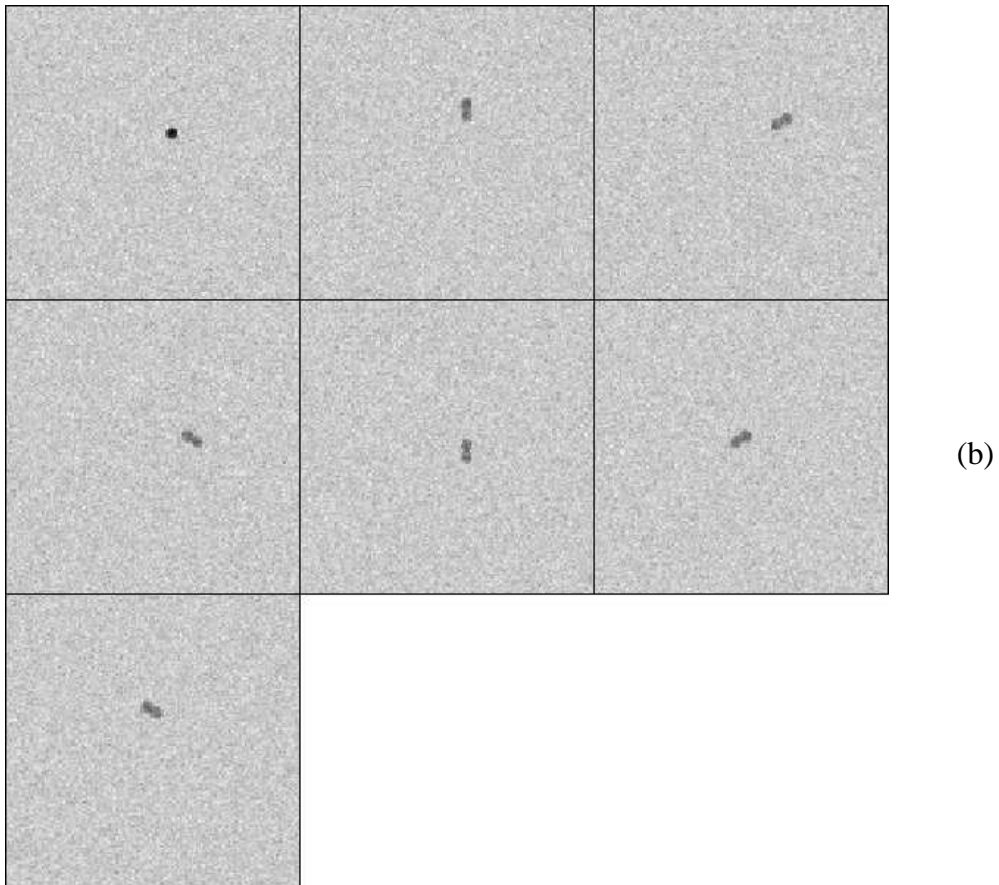
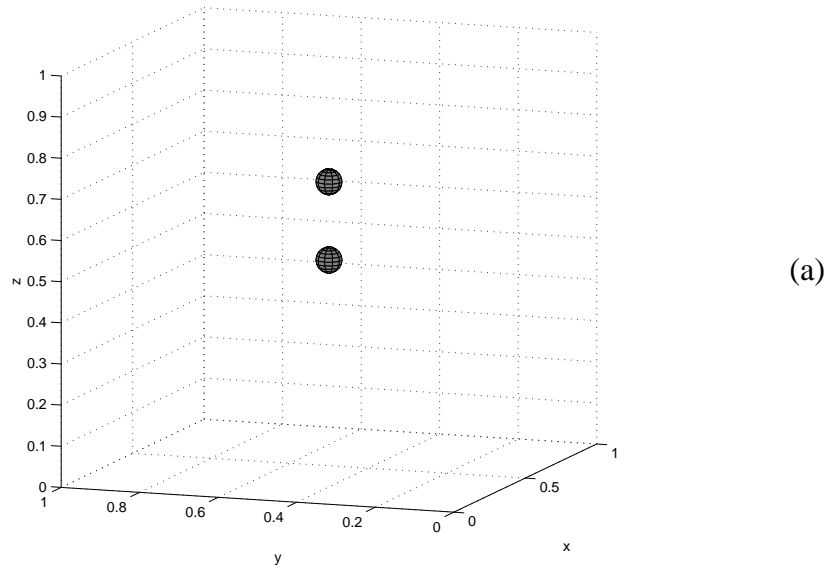


FIG. 4: Binary image to be reconstructed and seven noisy projections (SNR=  $-10$  dB). (a) The binary image is formed of two localized spherical objects of same size, centered at locations  $(0.5, 0.5, 0.5)$  and  $(0.5, 0.5, 0.69)$ , and of radius  $0.031$ . (b) The seven simulated radiographs computed from noisy cone-beam projections of image (a) onto the plane  $(z = 1)$ . Radiographs are gray level images formed of  $128 \times 128$  pixels. The darker gray levels correspond to the larger values.

monogrid and multigrid reconstruction methods by discussing the accuracy of the detection of the localized objects and the quality of the reconstructed image in terms of attenuation values and size of the reconstructed objects.

## B. Monogrid reconstruction

We first perform the monogrid reconstruction algorithm on a grid of  $32^3$  voxels yielded by a uniform sampling of the volume of interest  $[0, 1]^3$ . All displayed reconstructions are obtained with the data backprojection [Fig. 5 (a)] as initial solution and by performing only 50 iterations of the SSU algorithm, since the optimization task is numerically expensive. The results displayed in Fig. 5 are obtained with  $\lambda = 0$  and with two different values of  $\mu$ . For convenience, the two-dimensional (2D) central slice [plane of equation ( $x = 0.5$ )] of each reconstructed image is also shown, together with the slice of the two unknown spherical objects (bold circles in black or white). These results are promising, as they correctly localize the two objects that are not, however, fully discriminated. Selecting a large value of  $\mu$  clearly enhances the image sparsity, as the annealing of voxels is favored. However, the values of the localized object voxels are underestimated in comparison to their expected value ( $f_i^* = 1$ ), since the penalization term involved in criterion  $\mathcal{J}(\mathbf{f})$  is predominant with respect to the fidelity-to-data term. In particular, a large value of  $\mu$  such as  $\mu = 0.5$  yields the null image  $\hat{\mathbf{f}} = \mathbf{0}$ .

When the smoothness regularization is also taken into account (*i.e.*,  $\lambda \neq 0$ ), the threshold parameter  $T$  occurring in the hyperbolic function is set to  $T = 0.01$ . This selection is done relative to the prior knowledge of the range of the voxel values:  $f_i \in [0, 1]$ . Although a lower value of  $T$  further favors the appearance of sharp edges in the image, this choice leads to an "almost nondifferentiable" criterion  $\mathcal{J}(\mathbf{f})$ , since  $\phi(t)$  is equivalent to  $2T|t|$  when  $T \approx 0$ . This choice may thus slacken the decrease of series  $\{\mathcal{J}[\mathbf{f}(k)], k \geq 0\}$  during the optimization stage. The reconstructed images obtained while using two hyperparameters are represented on Fig. 6. We first set  $\mu$  to 0.01 and then tune the value of  $\lambda$ . Large values of  $\lambda$  yield a homogeneous image as well as a larger number of active voxels. Although increasing the image parametrization is desirable in order to prevent false detection of the background voxels, the use of smoothness regularization suffers from two drawbacks:

- the voxel values are underestimated. This behavior is similar to the influence of an overestimated value of  $\mu$ , as illustrated in Fig. 5;

- the size of the localized objects is overestimated along the vertical direction.

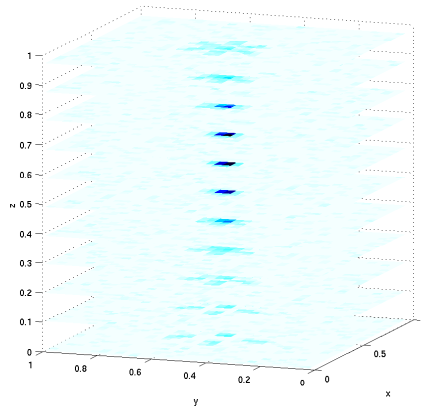
Fig. 7 (a) shows a reconstruction obtained on a  $64^3$  voxel grid while performing only 10 iterations of the SSU algorithm. For such fine grids, we need to reduce the number of iterations due to the very large computation time. Despite the large number of unknowns, the monogrid method provides very accurate reconstructions when using the annealing term only ( $\lambda = 0, \mu \neq 0$ ). On Fig. 7 (a), the two localized objects are clearly discriminated and their size and attenuation values are correctly estimated. In conclusion, the finer grid yields the best results in terms of discrimination of tiny localized objects, in spite of the large number of parameters to estimate.

Fig. 7 (b) illustrates the behavior of the monogrid reconstruction method in terms of computation time. For a fixed number of iterations, the method suffers from a drastic increase of the computation time when the grid resolution is fine. For the simulations of Figs. 5, 6, and 7 (a), the average overall CPU time amounts to 1856 s for the  $32^3$  voxel reconstructions (50 iterations of SSU), and to 2254 s for the  $64^3$  voxel reconstruction (10 iterations of SSU). Moreover, when performed on a fine resolved grid, the method necessitates the storage of a huge number of voxel values, and the projection matrix  $\mathbf{H}$ , of size  $M \times n = \{(7 \times 128^2) \times (64^3)\}$  cannot be stored. Although the SSU algorithm is implemented in such a way that the projection vector  $\mathbf{p} = \mathbf{H}\mathbf{f}$  is sequentially updated, we still need to recompute each matrix column  $\mathbf{H}_{\bullet i}$  when a voxel  $i$  is visited. On the contrary, sparse image representations enable the storage of  $\mathbf{H}$  when the number of active voxels is very limited, or at least that of a sparse image  $\mathbf{f}_a$  representing the discretization of the volume onto finer grids.

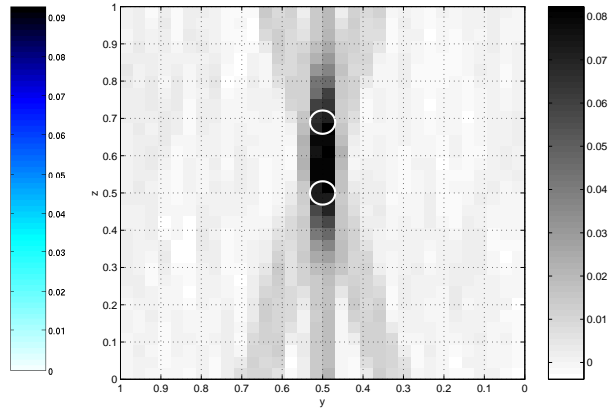
### C. Multigrid reconstruction

The multigrid reconstruction method alleviates the previous drawbacks by drastically reducing the image parametrization. We now exhibit the reconstructions obtained using the multigrid method by focusing on the sensitivity of the method to the two hyperparameters  $\lambda_1$  and  $\mu_1$  and to the given number of resolution levels. In the following, we aim at reconstructing a final fine resolved image of  $64^3$  voxels given, at the coarsest resolution level, a complete image parametrization  $\mathbf{f}^{(1)}$  formed of  $16^3$  voxels. The multigrid algorithm thus includes  $R = 3$  resolution levels.

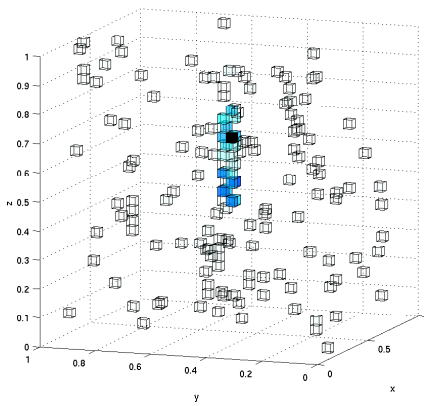
Let us recall that hyperparameters  $\lambda_1$  and  $\mu_1$  are empirically chosen at the coarsest level, and that (10) is the necessary and sufficient condition for the "image continuity" between two consecutive levels. Similarly to the monogrid case, parameters  $T_r$  are all set to 0.01 and we perform



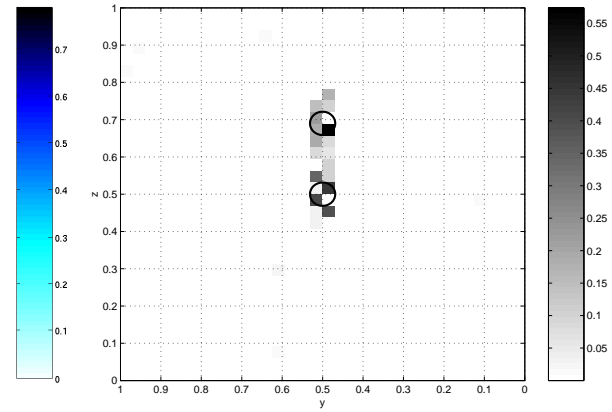
(a) Data backprojection



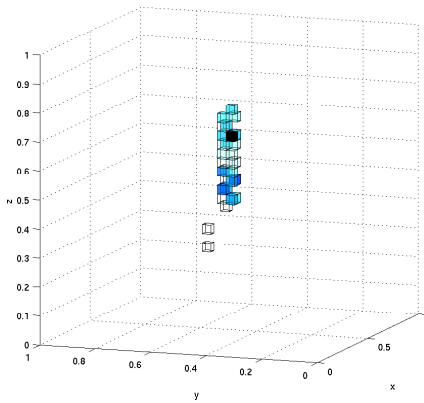
Central slice, of size  $32 \times 32$



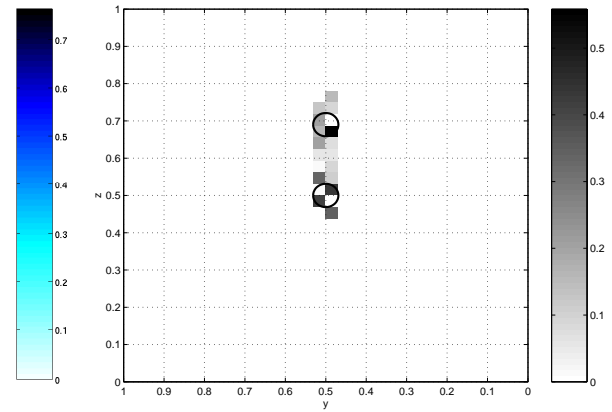
(b)  $\lambda = 0, \mu = 0.01$



Central slice

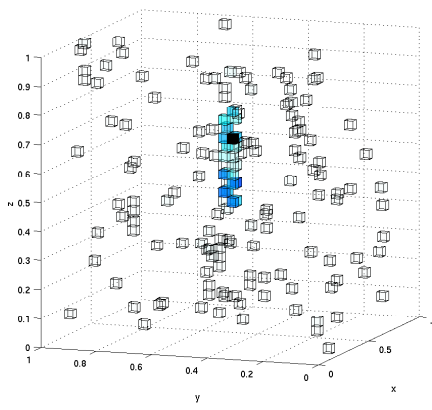


(c)  $\lambda = 0, \mu = 0.02$

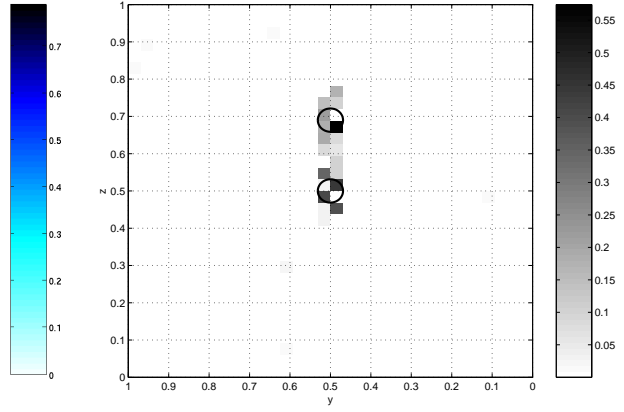


Central slice

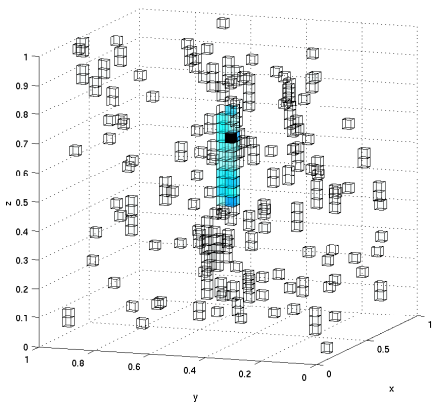
FIG. 5: Monogrid reconstruction formed of  $32^3$  voxels with 50 iterations of the SSU algorithm. (a) Data backprojection computed on the  $32^3$  voxel grid; for clarity, only 11 parallel slices are represented. (b-c) Monogrid reconstructions computed with (a) as initial solution and with a single penalization term ( $\lambda = 0, \mu \neq 0$ ), favoring annealing of the voxels. The null image is reconstructed when  $\mu$  is set to larger values (e.g.,  $\mu = 0.5$ ). The 2D images shown on the right column are the slices of the reconstructed images along the plane ( $x = 0.5$ ). The bold circles represent the shape of the unknown localized objects.



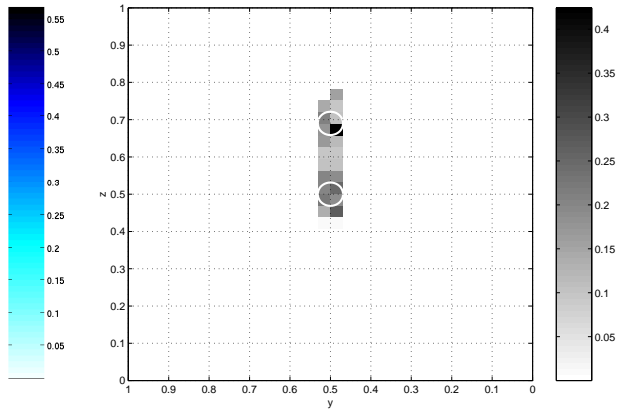
(a)  $\lambda = 0, \mu = 0.01$



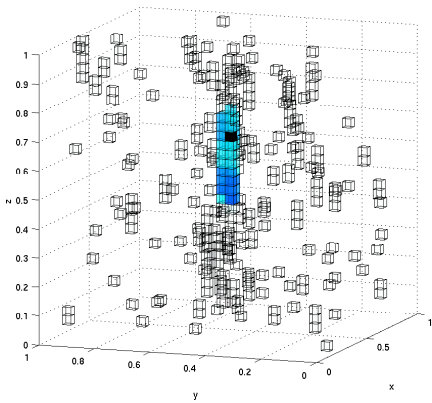
Central slice



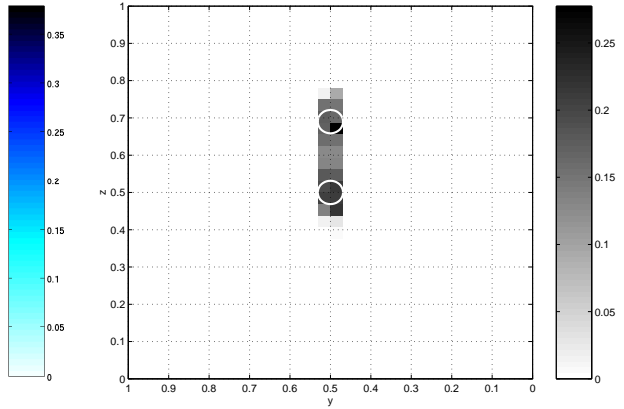
(b)  $\lambda = 0.05, \mu = 0.01$



Central slice

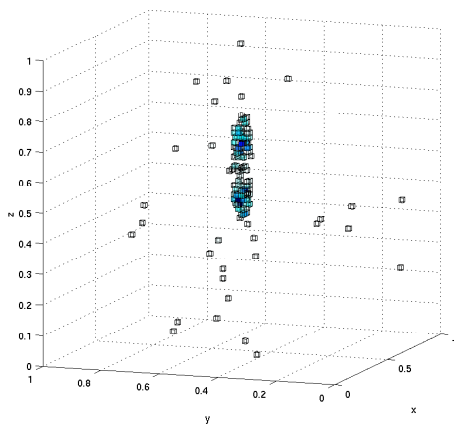


(c)  $\lambda = 0.1, \mu = 0.01$

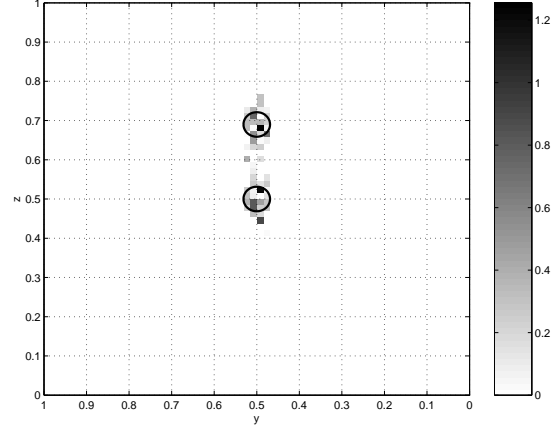


Central slice

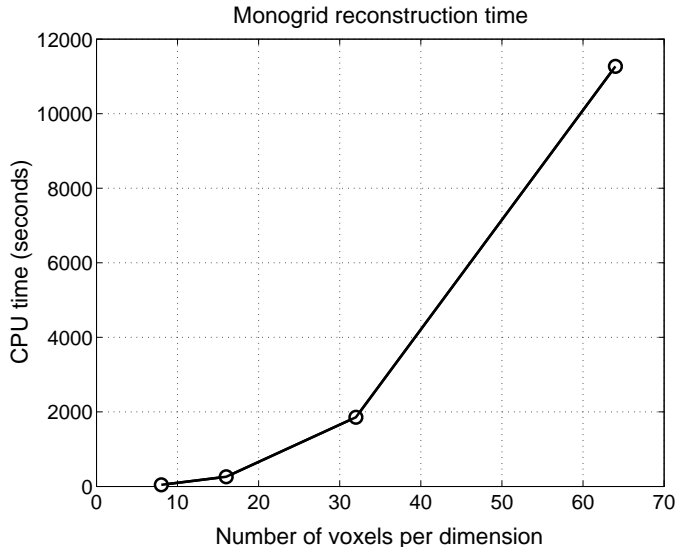
FIG. 6: Monogrid reconstruction formed of  $32^3$  voxels with 50 iterations of the SSU algorithm. The two penalization terms are utilized:  $\lambda, \mu \neq 0$ . The value of  $\mu$  is set to 0.01,  $T$  is set to 0.01, and  $\lambda$  is tuned to several values. (a-c) Monogrid reconstructions computed with the data backprojection as initial solution.



(a)  $\lambda = 0$ ,  $\mu = 0.004$



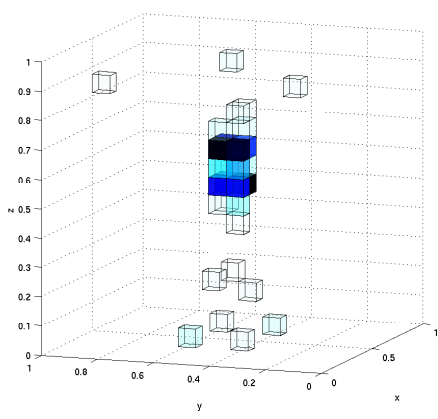
Central slice



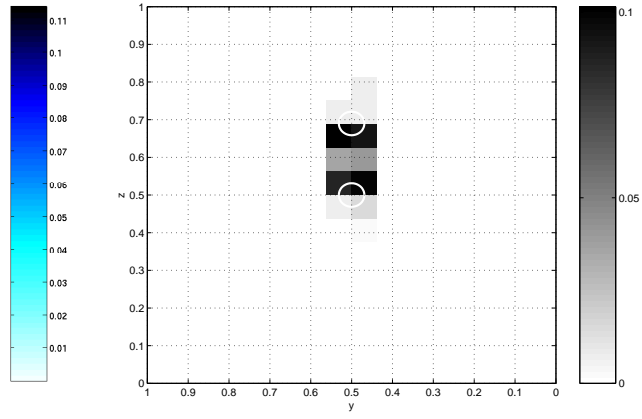
(b)

FIG. 7: (a) Monogrid reconstruction formed of  $64^3$  voxels with 10 iterations of the SSU algorithm. Only 1096 voxels, that is 0.05 % of the  $64^3$  voxels are not equal to 0. (b) Numerical time of computation for the monogrid reconstruction algorithm, expressed in seconds. Evaluation is done with respect to the resolution of the 3D image: successive reconstructions are done on grids of  $8^3$ ,  $16^3$ ,  $32^3$ , and  $64^3$  voxels, respectively. At each resolution,  $\lambda$  and  $\mu$  are empirically chosen, and 50 iterations of SSU are performed. For the  $64^3$  voxel grid, the numerical time is estimated based on the CPU time measured for 10 iterations of SSU.

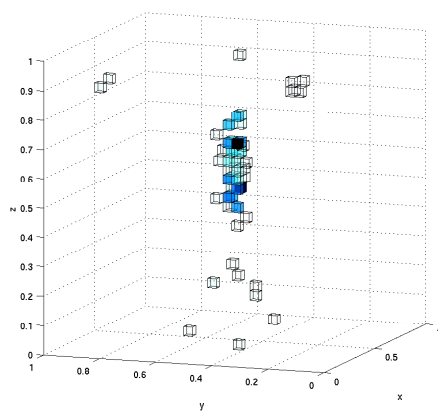
50 iterations of the SSU algorithm at level  $r = 1$ . We also perform 50 iterations per level when  $r > 1$  in order to compute the sparse images  $\hat{f}^{(2)}$  and  $\hat{f}^{(3)}$ . An increase of this number is generally possible within a reasonable computation time, provided that a large number of background voxels are detected at level  $r = 1$ .



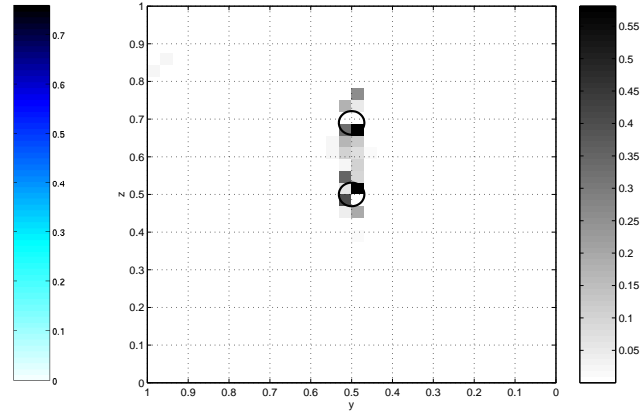
$16^3$  voxels,  $\lambda_1 = 0$ ,  $\mu_1 = 0.05$



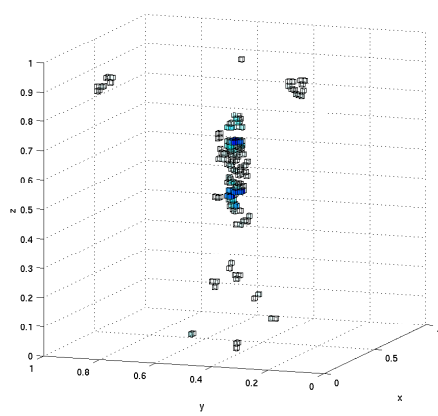
Central slice, of size  $16 \times 16$



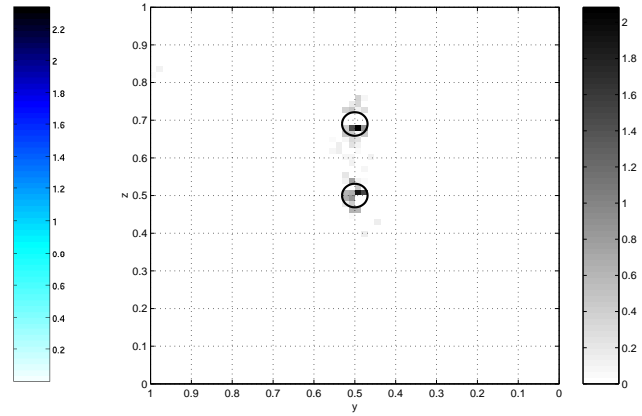
240 active voxels among  $32^3$  (0.73 %)



Central slice, of size  $32 \times 32$



440 active voxels among  $64^3$  (0.17 %)



Central slice, of size  $64 \times 64$

FIG. 8: Multigrid reconstruction on three levels, use of one penalization term only favoring the annealing of voxels:  $\lambda_r = 0$ ,  $\mu_r \neq 0$ . 50 iterations of the SSU algorithm are performed per resolution level.

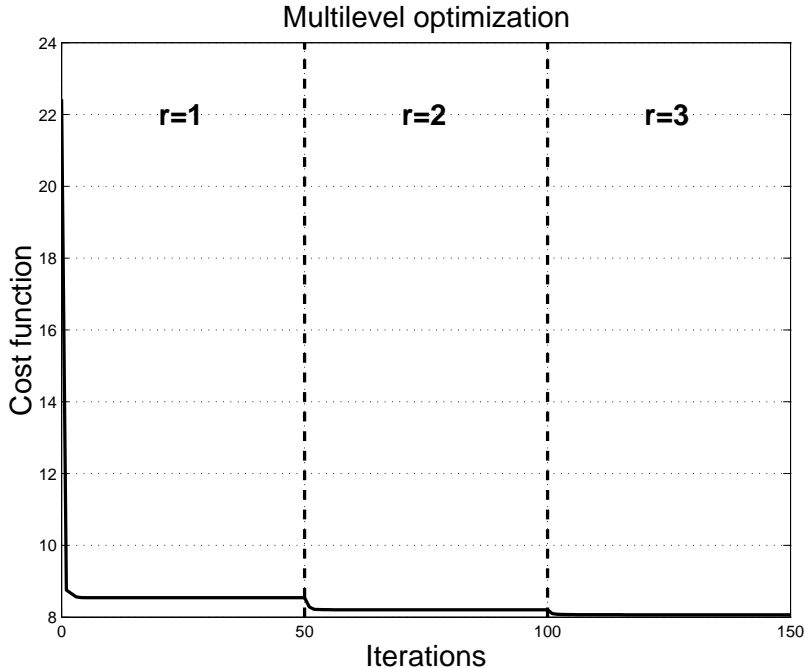


FIG. 9: Decrease of the cost function for the multigrid reconstruction of Fig. 8. Values of criterion  $\mathcal{J}_r[\mathbf{f}^{(r)}(k)]$  as a function of  $k$  ( $k = 1, \dots, 50$ ) at levels  $r = 1, 2, 3$ .

### 1. Regularization based on voxel annealing only

Fig. 8 displays the results obtained with  $R = 3$  levels. The coarsest grid reconstruction, formed of  $16^3$  voxels, is estimated from the data backprojection computed on the  $16^3$  voxel grid and using the annealing regularization only ( $\lambda_1 = 0$ ,  $\mu_1 = 0.05$ ). The multigrid algorithm efficiently discriminates both localized objects while affording a drastic reduction of the image parametrization at each resolution level. In particular, only 440 (*i.e.*, 0.17 %) of the  $64^3$  voxels are active at the finest level. For this reason also, the voxel values are more accurately reconstructed than in the monogrid case, because the indetermination of the limited angle reconstruction problem is partly alleviated by the image sparsity. However, the automatic rule  $\mu_r = \mu_1/8^{r-1}$  for selecting the annealing parameters generates a lot of nonnull voxels at fine resolution levels. Obviously, the value of  $\mu_r$  is tiny when the number of resolution levels is large, thus inactivating the annealing regularization. The same behavior is noticeable when the number of resolution levels is larger than  $R = 3$ .

Fig. 9 illustrates the behavior of the multigrid algorithm by showing the decrease of the cost function  $\mathcal{J}_r[\mathbf{f}^{(r)}(k)]$  with respect to  $r$  and  $k$  for the images reconstructed in Fig. 8. Although the

first optimization stage may require a large number of iterations to ensure the convergence of series  $\mathcal{J}_1[\mathbf{f}^{(1)}(k)]$ , the following optimization stages can often be carried out within a very few number of iterations, because initial solutions are accurate enough. Moreover, the latter stages are less consuming in terms of computation time per iteration due to the image sparsity. For the results shown in Fig. 8, the global time of reconstruction amounts to 305 s, that is 266, 15, and 24 s for each resolution level, respectively.

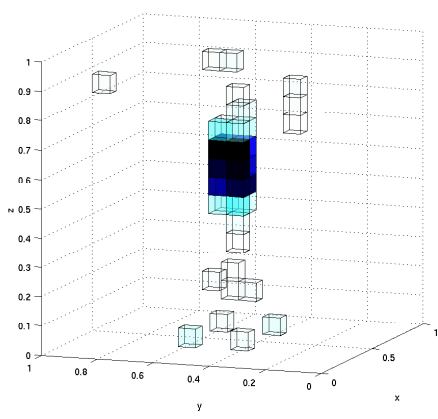
In Section V C 2, we utilize smoothness prior information in order to prevent the false detection of background voxels, on which the finer sparse image parametrizations depend.

## 2. Regularization based on smoothness and voxel annealing

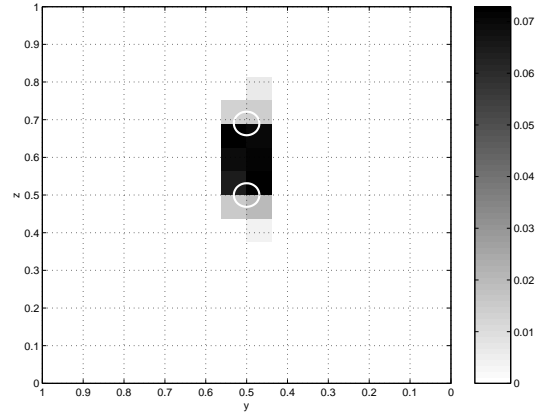
We obtain more accurate results using both smoothness and annealing regularizations. Obviously, the automatic rule  $\lambda_{r+1} = \lambda_r/4$ ,  $\mu_{r+1} = \mu_r/8$  implies that the annealing term of criterion  $\mathcal{J}_r$  is negligible with respect to the smoothness term for the finer grids. Moreover, we need to overestimate parameter  $\lambda_1$  at the coarsest level to keep it active at finer levels. Both penalizations are clearly inclined to be inactive if the number  $R$  of resolutions is set to a large value. Figure 10 displays the results obtained for  $R = 3$  levels. The value of  $\mu_1$  is set to 0.05 as in the simulation of Fig. 8, while  $\lambda_1$  is empirically selected and overestimated ( $\lambda_1 = 0.2$ ). This choice yields accurate results at the finest resolution level as the 2D central slice of the last reconstructed image displays a clear discrimination of the localized objects and accurate estimation of their size along both vertical and horizontal directions. The use of smoothness regularization avoids the appearance of isolated voxels, but on the other hand, it does not favor the detection of background voxels between both localized objects. For the results shown in Fig. 10, the number of active voxels is  $a_1 = 16^3 = 4096$ ,  $a_2 = 312$ , and  $a_3 = 856$  at each resolution level;  $a_2$  and  $a_3$  represent only 0.95 % and 0.33 % of the total number of voxels (*i.e.*,  $32^3$  and  $64^3$ ). The global time of reconstruction amounts to 321 s, that is 257, 19, and 45 s for each resolution level, respectively.

## D. Discussion

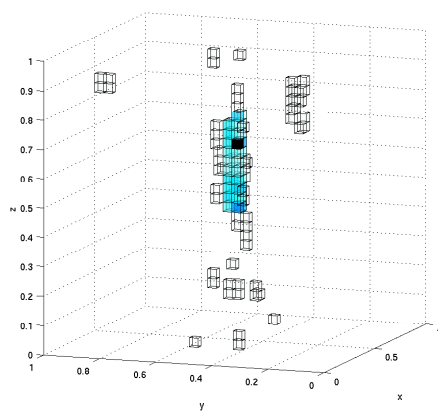
The difficulty of separation in the depth direction is the main problem raised by limited angle data. It is however possible to improve the regularization to add specific prior compensating for the lack of information in the depth direction.



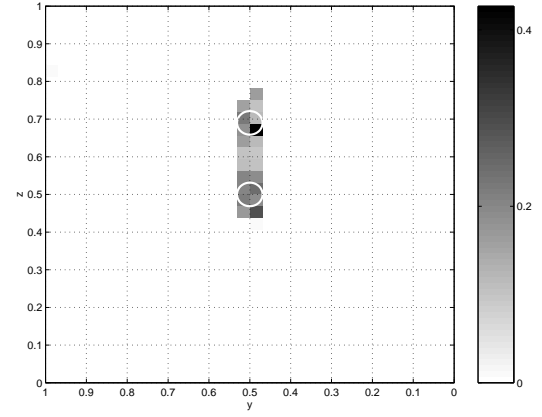
$16^3$  voxels,  $\lambda_1 = 0.2$ ,  $\mu_1 = 0.05$



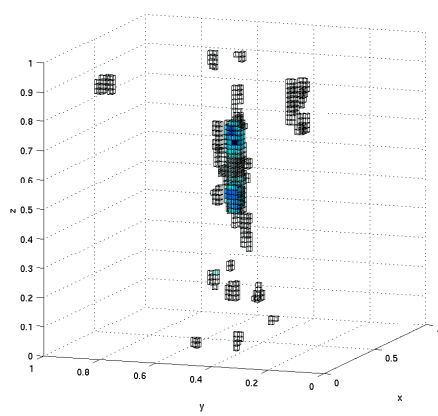
Central slice, of size  $16 \times 16$



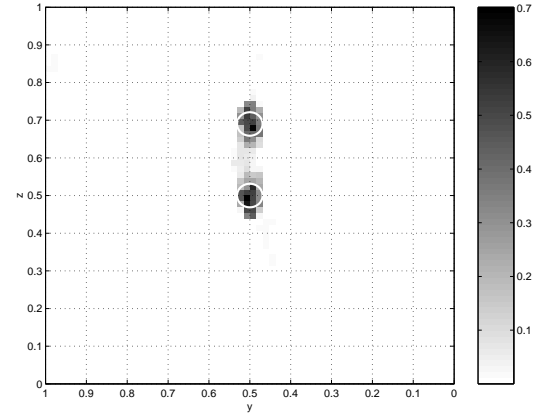
312 active voxels among  $32^3$  (0.95 %)



Central slice, of size  $32 \times 32$



856 active voxels among  $64^3$  (0.33 %)



Central slice, of size  $64 \times 64$

FIG. 10: Multigrid reconstruction on three resolution levels, use of two penalization terms:  $\lambda_r, \mu_r \neq 0$ . 50 iterations of the SSU algorithm are performed per resolution level, and  $T$  is set to 0.01.

In the presented method, the smoothness term  $\mathcal{D}(\mathbf{f}) = \sum_{i \sim j} \phi(f_i - f_j)$  is chosen isotropic, in

the sense that the neighborhood relation  $i \sim j$  is defined along the horizontal and vertical directions together ( $x$ -,  $y$ -, and  $z$ -axes). Each interior voxel  $f_i$  is thus involved into six terms  $\phi(f_i - f_j)$ . An interesting alternative to favor the discrimination of objects along the depth direction  $z$  is to use an anisotropic version in which the smoothness term does not have the same weight in the horizontal directions  $x$  and  $y$  and in the vertical direction. This can be achieved by adapting the value of  $T$  or  $\lambda$ , depending on the direction. In the following, we focus on the extreme case where only the horizontal interactions ( $f_i, f_j$ ) are considered (*i.e.*,  $\lambda = 0$  for vertical interactions). Each interior voxel  $f_i$  is now involved into four terms  $\phi(f_i - f_j)$  corresponding to its  $x$  and  $y$  neighbors. The monogrid and multigrid algorithms can be straightforwardly extended to the anisotropic case. In the monogrid case, the algorithms presented in Tables I and II are still valid as well as the update equations (6) and (7). The auxiliary variables  $b_{ij}$  are now defined for horizontal interactions  $i \sim j$  only. The multigrid algorithm of Table III can be extended in a similar fashion, while the rule (9) for recursive selection of the hyperparameters from one grid level to another is unchanged.

We performed a set of simulations in order to compare the isotropic and anisotropic algorithms, based on the data of Fig. 4. Qualitatively, the monogrid reconstruction results obtained with the anisotropic version are close to their isotropic counterparts, although for fixed values of  $\lambda_1$  and  $\mu_1$ , the range of the voxel values is more accurate in the anisotropic case. The voxel values are still underestimated, but larger than in the isotropic case. The reason for this result is that for a given value of  $\lambda_1$ , the number of terms involved in  $\mathcal{D}(f)$  is lower than in the isotropic case. Therefore, the number of active voxels is reduced at each resolution level, and the voxel values are increased in average. However, the anisotropic monogrid algorithm cannot clearly discriminate the localized objects, similarly to the isotropic algorithm.

We performed multigrid reconstructions on three levels similarly to the isotropic case. The anisotropic algorithm yields very accurate results in terms of discrimination and localization of the objects. When  $\lambda_1$  is chosen very large (*e.g.*,  $\lambda_1 = 2$ ), the anisotropic results remain of good quality while the isotropic version fails to discriminate the two objects. Let us stress that a large value of  $\lambda_1$  is a security, as the number of active voxels at each resolution level is important. On the contrary, when  $\lambda_1$  is set to a low value, the number of voxels that are detected as "background voxels" is larger, with the possibility that true localized object voxels are excluded.

In conclusion, we believe that the anisotropic adaptation of the reconstruction algorithms is of great interest to enhance the discrimination of objects along one specific direction. Not only the localized objects are better discriminated, but the results are also very robust with respect to the

smoothness parameter.

## VI. CONCLUSION

We have proposed a simple method adapted to the 3D reconstruction of one or several localized objects from a limited set of CT data. Both monogrid and multigrid approaches carry out the direct estimation of the image voxels in the MAP sense by using smoothness and/or voxel annealing assumptions. The annealing assumption permits the detection of a region of interest embedding the localized objects areas. When the monogrid image reconstruction is performed, we construct a sparse representation of the 3D volume, which partitions the image into a localized object region and a background region. The multigrid image reconstruction relies on a monogrid reconstruction done on a coarse image and a sequence of coarse-to-fine image reconstructions. These reconstructions involve, at each resolution level, the design of sparse image representations. We have shown that the monogrid reconstruction method yields accurate discrimination and reconstruction of the localized objects when the angles of projection are limited. The proposed regularization is also of interest in other more classical geometries of acquisition, in situations where the number of projections is low or the noise level is important. The multigrid extension provides a drastic reduction of the image parametrization at the finest levels as well as improved reconstructed images. In the case of multigrid image reconstruction, we recommend to use both smoothness and annealing regularizations and to overestimate the smoothness hyperparameter at the coarsest level in order to avoid the false detection of the background voxels and ensure the robustness of the reconstruction. The anisotropic extension presented in Section V D, in which the smoothness term does not have the same weight in the depth direction in comparison to the other directions, gives very promising discrimination results when the projection angles are limited.

At each resolution level, the MAP estimator of the voxels is computed by using a deterministic descent algorithm based on successive constrained optimizations with respect to one voxel at a time. We have shown on a set of simulations that the convergence of the algorithm is fast and that it is capable of detecting a large number of zero-valued voxels.

Future works will consist in improving the proposed method, namely, the optimization algorithm used for performing positive voxel estimation. First, replacing the set of constraints  $\mathbb{R}_+^n$  by the box  $[0, 1]^n$  is a trivial extension that may improve the accuracy of the estimation of the voxel values by taking advantage of the prior knowledge of their range. Second, the use of an interior

point approach based on the Lagrangian formulation of the constrained problem instead of the proposed SSU algorithm, would possibly improve the algorithm efficiency (see, for instance [48]). The minimization of  $\mathcal{J}$  under the positivity constraint could also benefit from recent advances in the field of variable selection based on the homotopy approach of [49]. In particular, the case when  $\lambda = 0$  or when  $\phi$  is chosen quadratic clearly enters the "positive-lasso" case of [50, p. 421] (see also [51] for a generalization including "Huber-like" penalty functions). Another strategy to carry out the optimization problem relies on its Bayesian formulation and on Monte Carlo techniques for sampling the voxel values. This approach has been recently introduced for positive image reconstruction problems [11] and yields promising results.

### Acknowledgments

This work was partially supported by Electricité de France (EDF) under Contract No. E961/P10AY0/E3. We thank the anonymous reviewers for their fruitful comments and suggestions.

- 
- [1] R. Zorgati, B. Duchêne, D. Lesselier, and F. Pons, "Eddy current testing of anomalies in conductive materials, part I: Qualitative imaging via diffraction tomography techniques", *IEEE Trans. Magnetics*, vol. 27, no. 6, pp. 4416–4437, 1991.
  - [2] A. B. Frakt, W. C. Karl, and A. S. Willsky, "A multiscale hypothesis testing approach to anomaly detection and localization from noisy tomographic data", *IEEE Trans. Image Processing*, vol. 7, no. 6, pp. 825–837, June 1998.
  - [3] L. Chatellier, L. Fournier, B. Charbonnier, L. Robillard, and B. Chassignole, "Characterization improvement through signal processing. Application to radiography inspection: 3D reconstruction", in *ASME Pressure Vessels and Piping Division Conference*, Denver, CO, July 2005.
  - [4] I. T. Rekanos and T. D. Tsiboukis, "An inverse scattering technique for microwave imaging of binary objects", *IEEE Trans. Microwave Theory Tech.*, vol. 50, no. 5, pp. 1439–1441, May 2002.
  - [5] F. Retraint, F. Peyrin, and J.-M. Dinten, "Three-dimensional regularized binary image reconstruction from three two-dimensional projections using a randomized ICM algorithm", *Int. J. Imag. Syst. Tech.*, vol. 9, no. 2-3, pp. 135–146, Dec. 1998.

- [6] C. A. Bouman and K. D. Sauer, “Nonlinear multigrid methods of optimization in Bayesian tomographic image reconstruction”, *Proc. of SPIE Conf. on Neural and Stochastic Methods in Image and Signal Processing*, vol. 1766, pp. 296–306, July 1992.
- [7] B. Chalmond, F. Coldefy, and B. Lavayssière, “Tomographic reconstruction from non-calibrated noisy projections in non-destructive evaluation”, *Inverse Problems*, vol. 15, pp. 399–411, 1999.
- [8] N. Robert, F. Peyrin, and M. J. Yaffe, “Binary vascular reconstruction from a limited number of cone beam projections”, *Medical Physics*, vol. 21, no. 12, pp. 1839–1851, Dec. 1994.
- [9] M. Allain and J. Idier, “Efficient binary reconstruction for non-destructive evaluation using gammagraphy”, *Inverse Problems*, vol. 23, no. 4, pp. 1371–1393, 2007.
- [10] J. A. Case, T.-S. Pan, M. A. King, D.-S. Luo, B. C. Penney, and M. S. Z. Rabin, “Reduction of truncation artifacts in fan beam transmission imaging using a spatially varying Gamma prior”, *IEEE Trans. Nuclear Sciences*, vol. 42, no. 6, pp. 2260–2265, Dec. 1995.
- [11] I.-T. Hsiao, A. Rangarajan, and G. Gindi, “Bayesian reconstruction for transmission tomography using deterministic annealing”, *J. Electr. Imag.*, vol. 2, no. 1, pp. 7–16, 2003.
- [12] S. Gautier, J. Idier, A. Mohammad-Djafari, and B. Lavayssière, “X-ray and ultrasound data fusion”, in *Proc. IEEE ICIP*, Chicago, IL, Oct. 1998, pp. 366–369.
- [13] K. D. Sauer and C. A. Bouman, “A local update strategy for iterative reconstruction from projections”, *IEEE Trans. Signal Processing*, vol. 41, no. 2, pp. 534–548, Feb. 1993.
- [14] S. Brette and J. Idier, “Optimized single site update algorithms for image deblurring”, in *Proc. IEEE ICIP*, Lausanne, Switzerland, Sept. 1996, pp. 65–68.
- [15] N. Villain, Y. Goussard, J. Idier, and M. Allain, “Three-dimensional edge-preserving image enhancement for computed tomography”, *IEEE Trans. Medical Imaging*, vol. 22, no. 10, pp. 1275–1287, Oct. 2003.
- [16] Y. Bresler and A. Macovski, “Three-dimensional reconstruction from projections with incomplete and noisy data by object estimation”, *IEEE Trans. Acoust. Speech, Signal Processing*, vol. ASSP-35, no. 8, pp. 1139–1152, Aug. 1987.
- [17] P. Milanfar, W. C. Karl, and A. S. Willsky, “Reconstructing binary polygonal objects from projections: A statistical view”, *Comput. Vision Graphics Image Process.*, vol. 56, no. 5, pp. 371–391, Sept. 1994.
- [18] K. M. Hanson, R. L. Bilisoly, and G. S. Cunningham, “Kinky tomographic reconstruction”, *Medical Imaging: Image Processing, Proc. SPIE*, vol. 2710, pp. 156–166, 1996.
- [19] X. L. Battle, C. Le Rest, A. Turzo, and Y. J. Bizais, “3D attenuation map reconstruction using geomet-

- rical models and free-form deformations”, *IEEE Trans. Medical Imaging*, vol. 19, no. 5, pp. 404–411, May 2000.
- [20] C. Soussen and A. Mohammad-Djafari, “Polygonal and polyhedral contour reconstruction in computed tomography”, *IEEE Trans. Image Processing*, vol. 13, no. 11, pp. 1507–1523, Nov. 2004.
- [21] F. Santosa, “A level-set approach for inverse problems involving obstacles”, *ESAIM : COCV*, vol. 1, pp. 17–33, Jan. 1996.
- [22] D. F. Yu and J. A. Fessler, “Edge-preserving tomographic reconstruction with nonlocal regularization”, *IEEE Trans. Medical Imaging*, vol. 21, no. 2, pp. 159–173, Feb. 2002.
- [23] H. Feng, W. C. Karl, and D. A. Castanon, “A curve evolution approach to object-based tomographic reconstruction”, *IEEE Trans. Image Processing*, vol. 12, no. 1, pp. 44–57, Jan. 2003.
- [24] J. G. Brankov, Y. Yang, and M. N. Wernick, “Tomographic image reconstruction based on content-adaptive mesh model”, *IEEE Trans. Medical Imaging*, vol. 23, no. 2, pp. 202–212, Feb. 2004.
- [25] L. Fillatre and I. Nikiforov, “Non-Bayesian detection and detectability of anomalies from a few noisy tomographic projections”, *IEEE Trans. Signal Processing*, vol. 55, no. 2, pp. 401–413, Feb. 2007.
- [26] T. Olson and J. DeStefano, “Wavelet localization of the Radon transform”, *IEEE Trans. Signal Processing*, vol. 42, no. 8, pp. 2055–2067, Aug. 1994.
- [27] A. H. Delaney and Y. Bresler, “Multiresolution tomographic reconstruction using wavelets”, *IEEE Trans. Image Processing*, vol. 4, no. 6, pp. 799–813, June 1995.
- [28] F. Rashid-Farrokhi, K. J. Ray Liu, C. A. Berenstein, and D. Walnut, “Wavelet-based multiresolution local tomography”, *IEEE Trans. Image Processing*, vol. 6, no. 10, pp. 1412–1430, Oct. 1997.
- [29] S. Bonnet, F. Peyrin, F. Turjman, and R. Prost, “Multiresolution reconstruction in fan-beam tomography”, *IEEE Trans. Image Processing*, vol. 11, no. 3, pp. 169–176, Mar. 2002.
- [30] M. V. Ranganath, A. P. Dhawan, and N. Mullani, “A multigrid expectation maximization reconstruction algorithm for positron emission tomography”, *IEEE Trans. Medical Imaging*, vol. 7, no. 4, pp. 273–278, Dec. 1988.
- [31] T.-S. Pan and A. E. Yagle, “Numerical study of multigrid implementations of some iterative image reconstruction algorithms”, *IEEE Trans. Medical Imaging*, vol. 10, no. 4, pp. 572–588, Dec. 1991.
- [32] W. Zhu, Y. Wang, Y. Deng, Y. Yao, and R. L. Barbour, “A wavelet-based multiresolution regularized least squares reconstruction approach for optical tomography”, *IEEE Trans. Medical Imaging*, vol. 16, no. 2, pp. 210–217, Apr. 1997.
- [33] J. C. Ye, C. A. Bouman, K. J. Webb, and R. P. Millane, “Nonlinear multigrid algorithms for Bayesian

- optical diffusion tomography”, *IEEE Trans. Image Processing*, vol. 10, no. 6, pp. 909–922, June 2001.
- [34] S. Oh, A. B. Milstein, C. A. Bouman, and K. J. Webb, “A general framework for nonlinear multigrid inversion”, *IEEE Trans. Image Processing*, vol. 14, no. 1, pp. 125–140, Jan. 2005.
- [35] S. S. Saquib, C. A. Bouman, and K. D. Sauer, “A non-homogeneous MRF model for multiresolution Bayesian estimation”, in *Proc. IEEE ICIP*, Lausanne, Switzerland, Sept. 1996, vol. 2, pp. 445–448.
- [36] T. Frese, C. A. Bouman, and K. D. Sauer, “Adaptive wavelet graph model for Bayesian tomographic reconstructions”, *IEEE Trans. Image Processing*, vol. 11, no. 7, pp. 756–770, July 2002.
- [37] K. Sauer and J.-B. Thibault, “Imaging from low-intensity data”, in *Bayesian Approach to Inverse Problems*, J. Idier, Ed. Apr. 2008, pp. 357–374, ISTE Ltd and John Wiley & Sons Inc.
- [38] C. A. Bouman and K. D. Sauer, “A unified approach to statistical tomography using coordinate descent optimization”, *IEEE Trans. Image Processing*, vol. 5, no. 3, pp. 480–492, Mar. 1996.
- [39] J. A. Fessler, “Penalized weighted least-squares image reconstruction for positron emission tomography”, *IEEE Trans. Medical Imaging*, vol. 13, no. 2, pp. 290–300, 1994.
- [40] M. E. Davison, “The ill-conditioned nature of the limited angle tomography problem”, *SIAM J. Appl. Mathematics*, vol. 43, no. 2, pp. 428–448, Apr. 1983.
- [41] M. Nikolova and M. K. Ng, “Analysis of half-quadratic minimization methods for signal and image recovery”, *SIAM J. Sci. Comput.*, vol. 27, no. 3, pp. 937–966, Dec. 2005.
- [42] C. Soussen and J. Idier, “3D reconstruction of localized objects from radiographs and based on multiresolution and sparsity”, in *Proc. IEEE ICIP*, Genova, Italy, Sept. 2005, vol. III, pp. 744–747.
- [43] D. P. Bertsekas, *Nonlinear programming*, Athena Scientific, Belmont, MA, 2 edition, 1999.
- [44] D. Geman and G. Reynolds, “Constrained restoration and the recovery of discontinuities”, *IEEE Trans. Pattern Anal. Mach. Intell.*, vol. 14, no. 3, pp. 367–383, Mar. 1992.
- [45] J. Idier, “Convex half-quadratic criteria and interacting auxiliary variables for image restoration”, *IEEE Trans. Image Processing*, vol. 10, no. 7, pp. 1001–1009, July 2001.
- [46] R. T. Rockafellar, *Convex Analysis*, Princeton Univ. Press, 1970.
- [47] J. Arvo, *Graphics Gems II*, Academic Press, 1991.
- [48] C. A. Johnson, J. Seidel, and A. Sofer, “Interior-point methodology for 3-D PET reconstruction”, *IEEE Trans. Medical Imaging*, vol. 19, no. 4, pp. 271–285, Apr. 2000.
- [49] M. R. Osborne, B. Presnell, and B. A. Turlach, “A new approach to variable selection in least squares problems”, *IMA Journal of Numerical Analysis*, vol. 20, no. 3, pp. 389–403, 2000.
- [50] B. Efron, T. Hastie, I. Johnstone, and R. Tibshirani, “Least angle regression”, *Annals Statist.*, vol. 32,

no. 2, pp. 407–451, 2004.

- [51] S. Rosset and J. Zhu, “Discussion of "Least angle regression" by B. Efron, T. Hastie, I. Johnstone and R. Tibshirani”, *Annals Statist.*, vol. 32, no. 2, pp. 469–475, 2004.
- [52] The X-ray projection of image  $f^*(x, y, z)$  only depends on the intersections between each projection line and the surface of both spherical objects. The calculus of those intersections can be done analytically from the spherical shape description, with no use of a voxel approximation of function  $f^*(x, y, z)$  [47].

### Biographies of the authors

Charles Soussen was born in France in 1972. He received the degree from the École Nationale Supérieure en Informatique et Mathématiques Appliquées, Grenoble, France, and the PhD degree in Physics from the Laboratoire des Signaux et Systèmes, Université de Paris-Sud, Orsay, France in 1996 and 2000, respectively. He currently is an Assistant Professor at the Université Henri Poincaré, Nancy-I, France. His research interests are in inverse problems and image reconstruction.

Jérôme Idier was born in France in 1966. He received the diploma degree in electrical engineering from École Supérieure d’Électricité, Gif-sur-Yvette, France in 1988 and the Ph.D. degree in physics from University of Paris-Sud, Orsay, France in 1991.

Since 1991, he joined the Centre National de la Recherche Scientifique. He is currently Senior Researcher at the Institut de Recherche en Communications et Cybernétique in Nantes. His major scientific interests are in probabilistic approaches to inverse problems for signal and image processing.



FIG. 11: Photographs of the authors